Computational Analysis in Support of the CRM Tail Cone Thruster Configuration Wind Tunnel Test*

Luis S. Fernandes†, Leonardo G. Machado†, Jared C. Duensing and Cetin C. Kiris
Computational Aerosciences Branch
NASA Ames Research Center

Advanced Modeling & Simulation (AMS) Seminar Series
NASA Ames Research Center, January 20th, 2022

† *Science & Technology Corporation*

*AIAA-2022-1171 – AIAA SciTech Conference January 2022

Outline

- Introduction
  - Motivation and objectives
  - Wind tunnel test article
  - Computational approach
- Validation study
- Database runs
  - Grid refinement study
  - Flow distortion sensitivity studies to flow conditions
- CFD support for inlet guide vane design and integration
  - CFD results from design iteration studies
  - Propulsor model thrust profile sensitivity study
- Summary and next steps

INTRODUCTION

Motivation

- One of the objectives of NASA's Advanced Air Transport Technology (AATT) project is to explore and design key enabling technologies for subsonic fixed wing aircraft with dramatically reduced fuel burn
  - Boundary layer ingesting (BLI) propulsion systems are one of the technologies currently being considered
  - Different propulsion-airframe integration (PAI) strategies result in two types of BLI

Double bubble D8. Credit: NASA

STARC-ABL propulsion system. Credit: NASA

Motivation

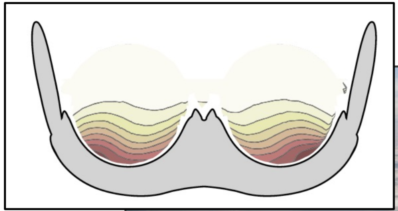

Courtesy of Shishir Pandya (NASA)

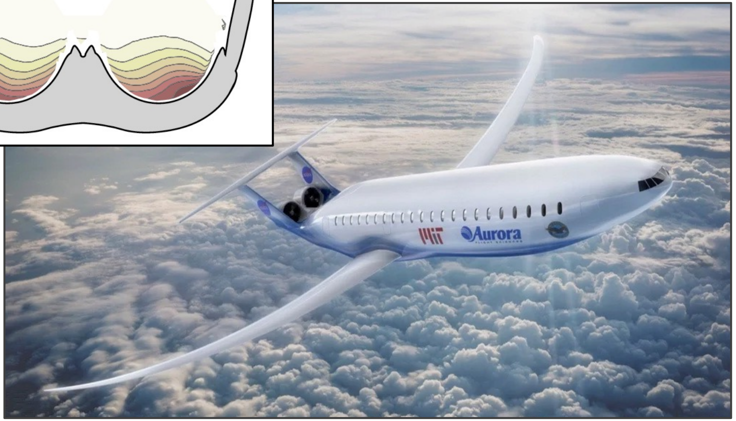

Double bubble D8. Credit: NASA

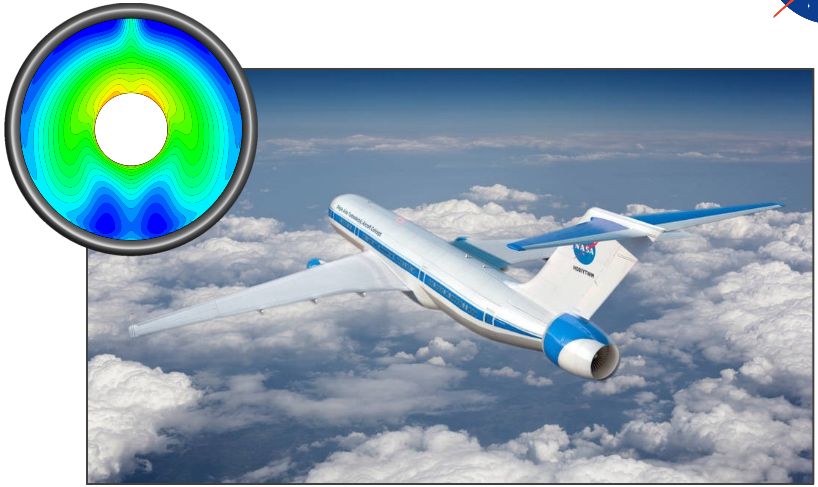

STARC-ABL propulsion system. Credit: NASA

- Inlet distortion signature containing a lower total pressure region with large variation in swirl over the bottom half of the engine inlet
- Top half of engine inlet ingests mainly freestream air with little to no distortion

- Engine installed at closeout of the fuselage
- Inlet distortion signature characterized by lower total pressure region near the hub, with clusters of low total pressure and high-swirl flow resulting from the combined effect of vertical tail wake, wing downwash and fuselage upsweep

System Level Benefits of BLI Propulsion

- At a system level, the benefits of BLI are two-fold
  - Increased propulsive efficiency, resulting from the lower jet dissipation losses that stem from lower engine inlet and jet exhaust velocities, due to ingestion of low-speed boundary layer flow
  - Lower weight and drag, resulting from the level of propulsion-airframe integration (PAI) offered by BLI, with potential to benefit noise shielding
  - Hardin et al. [1] report a 3-5% reduced fuel burn using BLI
  - Hall et al. [2] use control volume analyses to present a breakdown of the dissipation mechanisms that the power added by the propulsor balances, and report a 9% lower mechanical power required by an engine using BLI on the D8 aircraft concept
- Validation of CFD tools to allow high-fidelity simulations of concepts employing BLI will be key in refining these low-order estimates

[1] doi.org/10.2514/6.2012-3993
[2] doi.org/10.2514/1.B36321

Objectives

Part I

- Generate CFD database in preparation for the upcoming Common Research Model Tail Cone Thruster (CRM-TCT) test in the National Transonic Facility (NTF) at NASA LaRC using the LAVA solver framework
- Identify key flow features contributing to flow distortion upstream of the BLI fan
- Document flow distortion sensitivities to aircraft operating conditions and wind tunnel hardware

Part II

- Support integration of an inlet guide vane (IGV) system capable of mitigating the flow distortion at the engine inlet, in collaboration with TURBO team at NASA GRC

Objectives

This work **does not** mean to accomplish:

- An assessment of the benefits/compromises of an aircraft employing BLI, compared to a traditional underwing engine configuration
- An indication of the BLI benefit in terms of a reduction in fuel burn
  - ☞ These will come in at a later stage in the context of high-fidelity CFD

Instead, we want to **answer**:

- Can our current computational tools accurately predict the physical features of flows with BLI technology?
- What flow features is our CFD doing a good job at capturing, and which ones can it improve upon?

Background on NTF CRM-TCT Wind Tunnel Test

- 2.7% scale CRM has been retrofitted with a tail cone thruster (CRM-TCT) and will be tested in the NTF in 2022
  - Test will identify sensitivity of key flow distortion metrics at the engine inlet to angle of attack, Mach and Reynolds numbers, and engine operating power level
  - Serve as a database for benchmarking CFD solvers
  - First step in a series of test campaigns towards understanding and overcoming the challenges associated with installing a BLI fan subject to flow distortion

CRM-TCT Wind Tunnel Test Articles

- Four distinct configurations were designed*

Supporting
Strut (**Sting**)

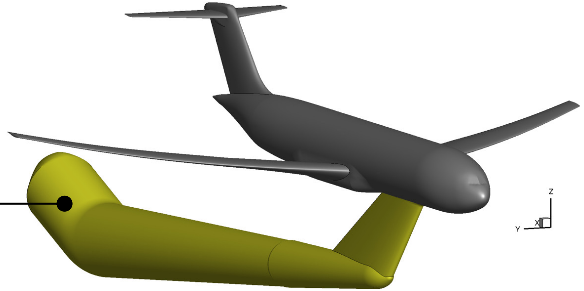

Clean, sting configuration (Clean-S)

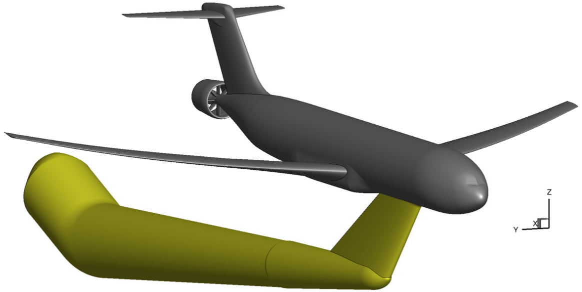

TCT, sting configuration (TCT-S)

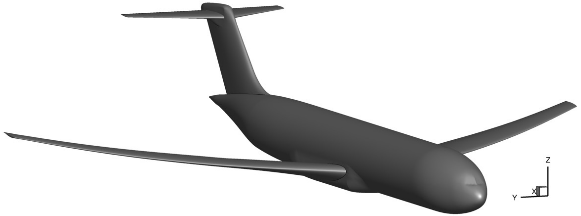

Clean, no sting configuration (Clean-NS)

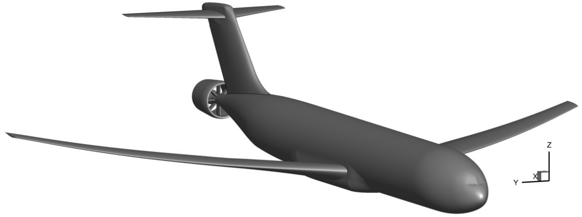

TCT, no sting configuration (TCT-NS)

* Courtesy of Greg Jones (NASA LaRC)

CRM-TCT Wind Tunnel Test Articles

- Differences in aft-body between clean and TCT configuration

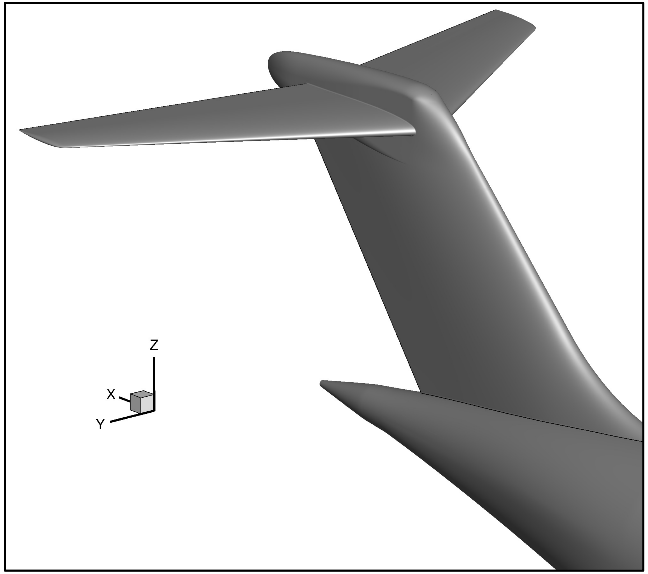

Clean configuration aft-body.

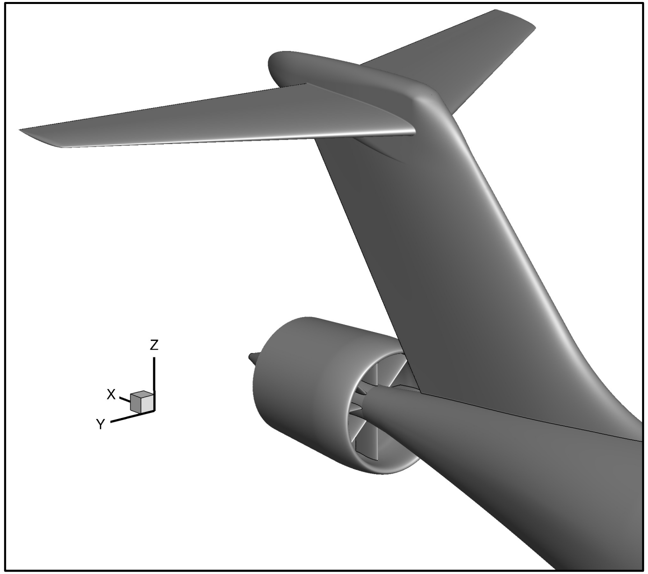

TCT configuration aft-body.

CRM-TCT Wind Tunnel Test Articles

- Three unique mass flow plugs (MFP) will test the sensitivity of flow distortion parameters to the engine operating power level

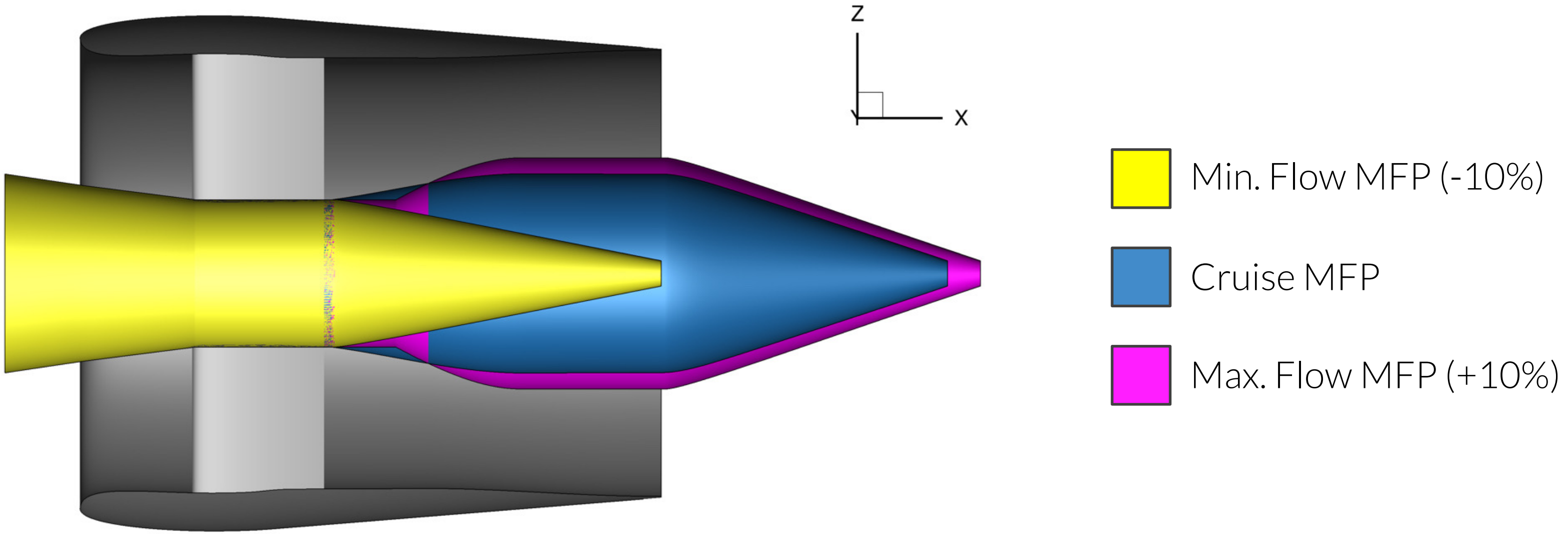

Mass flow plugs profile comparison

CRM-TCT Wind Tunnel Test Matrix

- Test matrix composed of 240 cases in total

Reynolds Number	Mach Number	Angle of Attack (deg)	Mass Flow Plug	Configuration
5M , 10M , 20M	0.75, 0.80, 0.85	-3, -2, -1, 0, 1, 2, 3, 4	-	Clean-NS
5M , 10M , 20M	0.75, 0.80, 0.85	-3, -2, -1, 0, 1, 2, 3, 4	Cruise	TCT-NS
5M , 10M , 20M	0.75, 0.80, 0.85	-2, 0, 2, 4	-10%	TCT-NS
5M , 10M , 20M	0.75, 0.80, 0.85	-2, 0, 2, 4	+10%	TCT-NS
10M	0.75, 0.80, 0.85	-2, 0, 2, 4	Cruise	Clean-S
10M	0.75, 0.80, 0.85	-2, 0, 2, 4	Cruise	TCT-S

NS – No Sting
S – Sting

LAVA CFD Solver Framework

- All 240 cases were simulated using the Launch, Ascent, and Vehicle Aerodynamics (LAVA) solver framework
- A finite difference formulation is applied to the compressible curvilinear RANS equations in strong conservation law form and solved using a set of structured curvilinear overset grid systems
- Spalart-Allmaras (SA) turbulence model with Rotation/Curvature corrections and Quadratic Constitutive Relation for the stress tensor is used (SA RC-QCR2000)
- 2nd order convective flux discretization, consisting of a modified Roe scheme with third order left/right state reconstruction and a Koren limiter

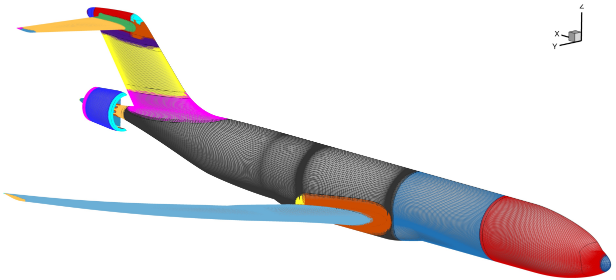

Overset surface grids over the CRM-TCT

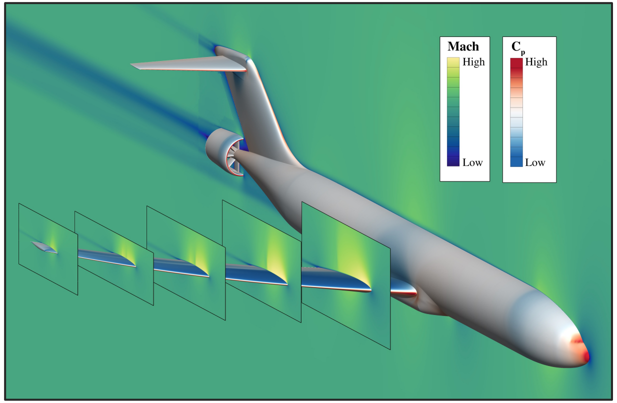

Flow visualization showing Mach and C_p contours

VALIDATION STUDY (DPW-VI)

Drag Prediction Workshop (DPW) VI Validation Study

- Two cases from DPW-VI were selected for validation of the LAVA overset curvilinear solver in the present work, for two reasons
  - CRM-TCT model is based on the CRM model used in DPW-VI
  - Large array of experimental data collected in different wind tunnels is available
- Two configurations of the CRM were considered
  - Wing + Body (WB)
  - Wing + Body + Nacelle + Pylon (WBNP)
- DPW-VI case 2 and case 3

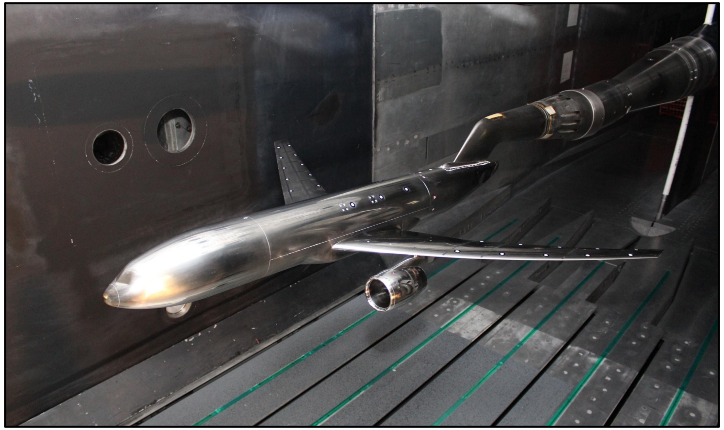

Common Research Model (CRM). https://aiaa-dpw.larc.nasa.gov

DPW-VI Validation Study

Case 2 – Compute the drag increment between the WB and WBNP configurations at a fixed C_L of 0.5

- Mach = 0.85, Re_c = 5M
- Family of 6 parametrically equivalent grids constructed for grid refinement study
- Broyden solver in LAVA used to target C_L of 0.5 using the angle-of-attack as output
- Spalart-Allmaras (SA) turbulence model enhanced with RC-QCR2000 corrections

Grid Level	Viscous Spacing (in)	Average Wall y^+	Max. SR*	# Grid Pts. (WB)	# Solve Pts. (WB)	# Grid Pts. (WBNP)	# Solve Pts. (WBNP)
Tiny	0.014780	1.02	1.235	7,398,176	6,379,336	11,865,177	9,707,120
Coarse	0.011820	0.80	1.186	14,355,678	12,497,390	22,999,565	18,990,993
Medium	0.009853	0.67	1.149	24,698,828	21,630,582	39,542,953	30,803,381
Fine	0.008446	0.58	1.128	39,098,858	34,394,846	62,566,221	52,167,031
Extra-Fine	0.007390	0.50	1.112	58,227,000	51,400,952	93,176,522	77,942,776
Ultra-Fine	0.006569	0.45	1.099	82,754,486	73,222,123	132,381,764	110,984,107

* SR – Stretching ratio

DPW-VI Validation Study

- Strong 2nd order convergence observed for the drag coefficient C_D
- Drag increment ΔC_D trend observed to fall within experimental uncertainty range

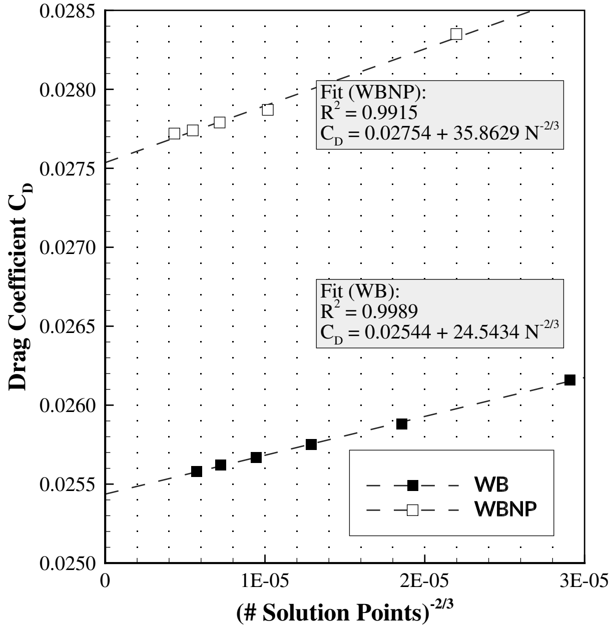

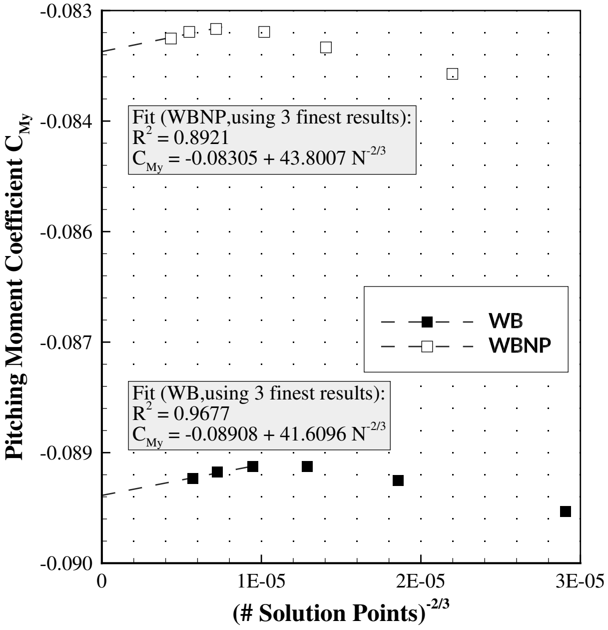

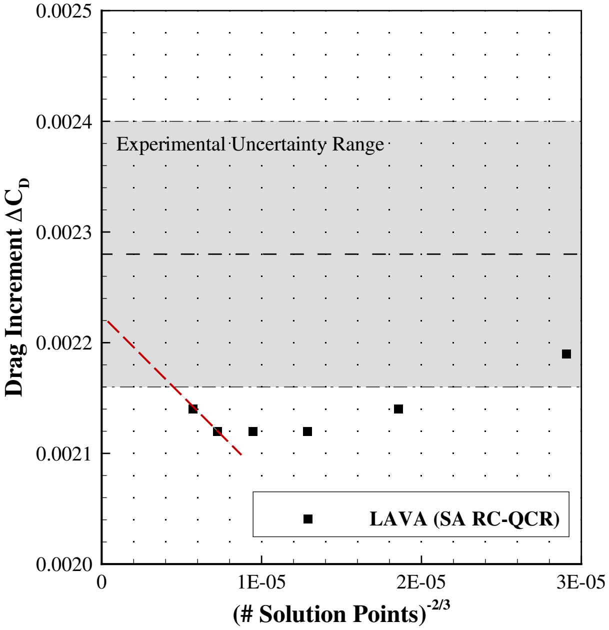

DPW-VI Validation Study

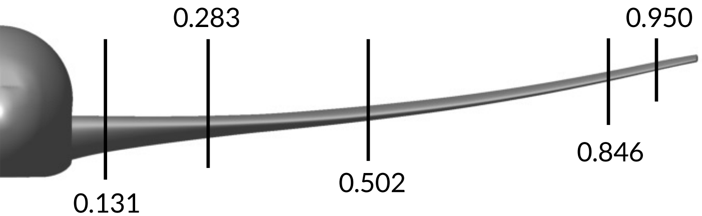

LAVA (WB, SA RC-QCR, Ultra-Fine) 82M
NTF T197R44, C_L = 0.487 (WB)
NTF T197R44, C_L = 0.521 (WB)
Ames 11ft T216R126, C_L = 0.482 (WB)
Ames 11ft T216R126, C_L = 0.518 (WB)

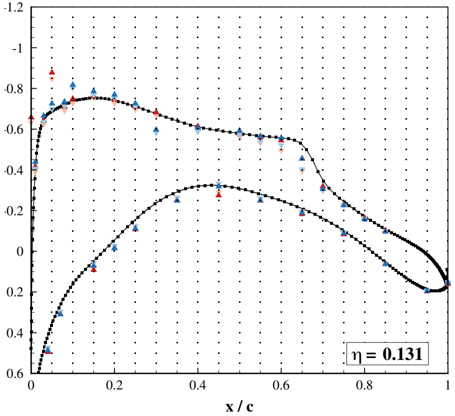

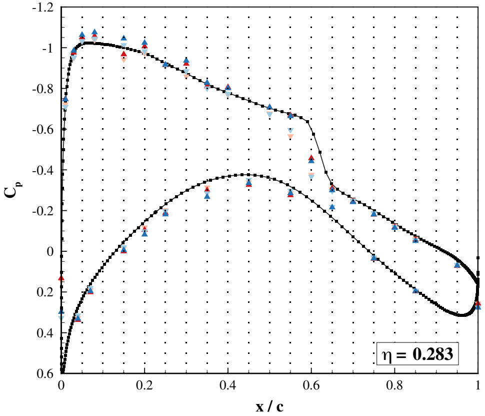

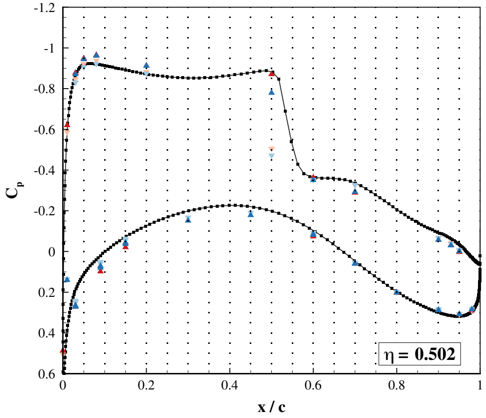

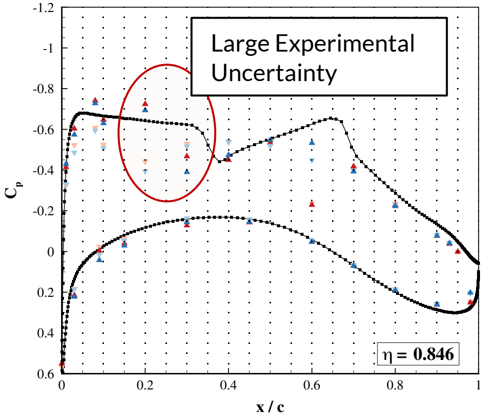

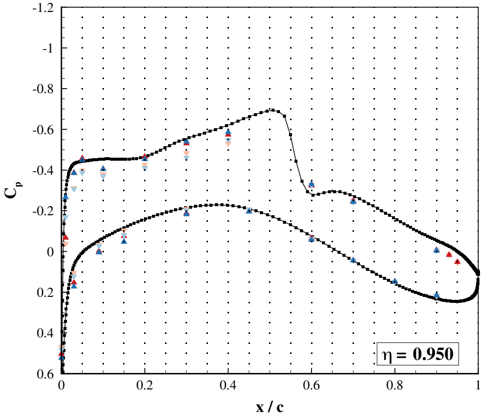

DPW-VI Validation Study

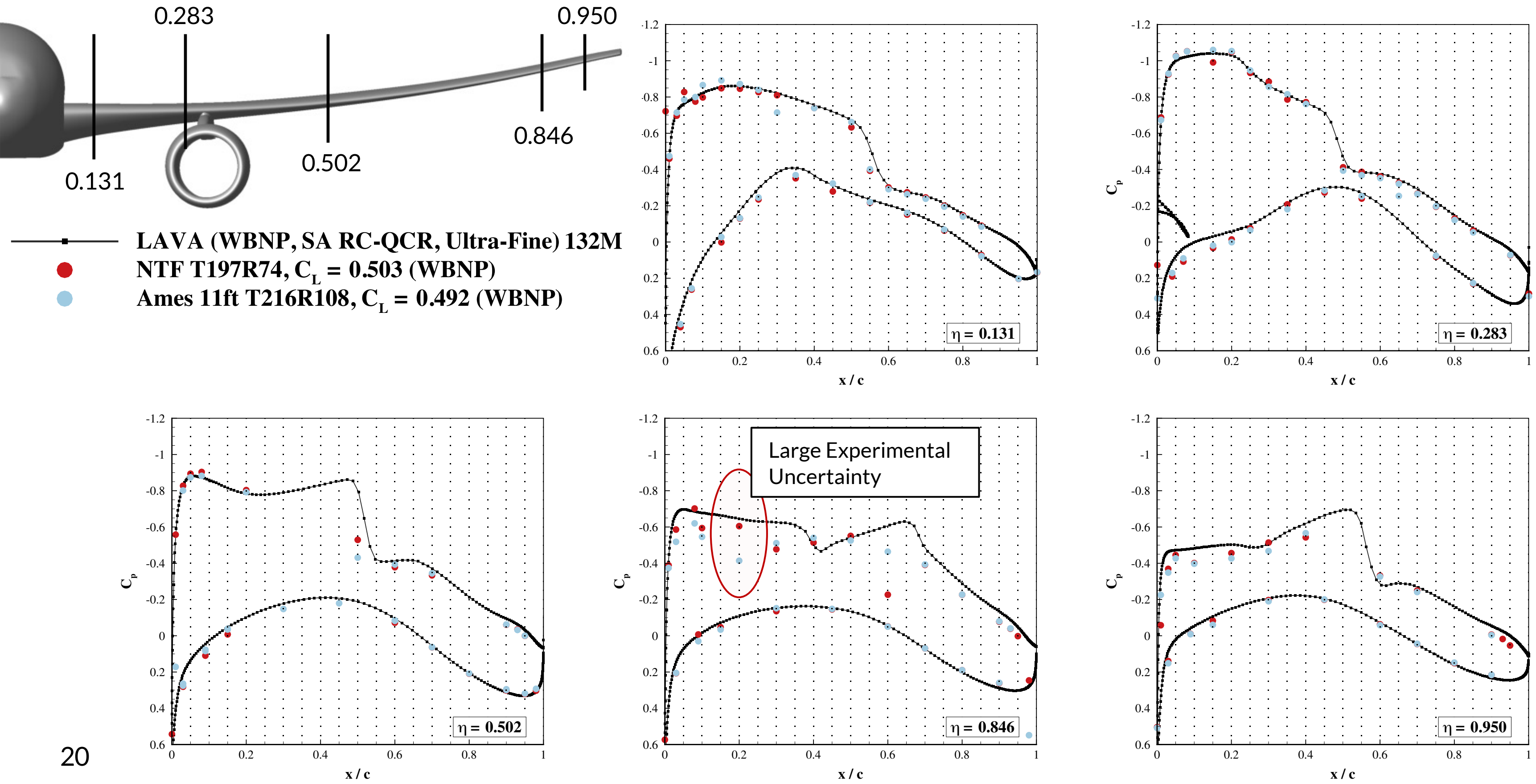

DPW-VI Validation Study

Case 3 – Perform an angle-of-attack sweep on the WB configuration, taking into account the wing deflections measured in the European Transonic Wind tunnel (ETW)

- Medium grid refinement level (25M)
- Angles-of-attack (AoA) ranging between 2.5° and 4°, in 0.25° increments
- Wing grids modified at each AoA according to aeroelastic deflections measured in ETW

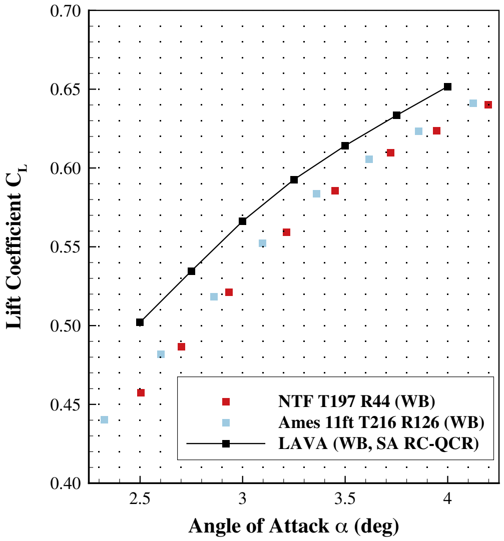

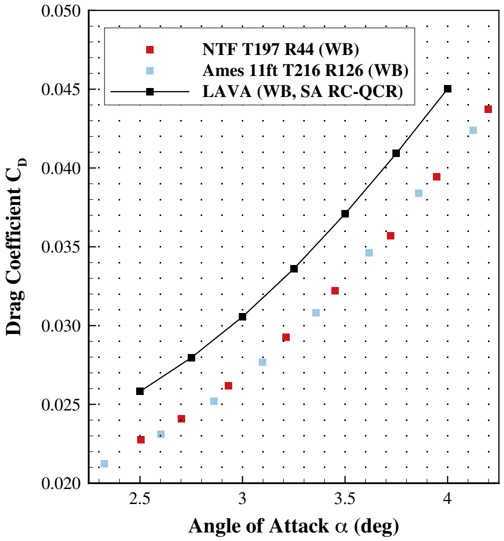

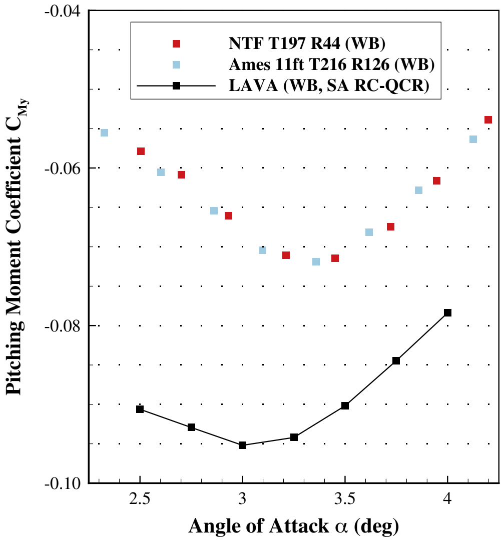

DPW-VI Validation Study

- LAVA solver results are among the best workshop-submitted SA-QCR results
- Discrepancy between wind tunnel data and CFD results partially attributed to lack of a corrected wind tunnel dataset accounting for mounting hardware effects[3]
- Computational studies on the impact of the sting on the loads on a CRM model with a horizontal tail† show a decrease in lift and an increase in pitching moment[4,5]

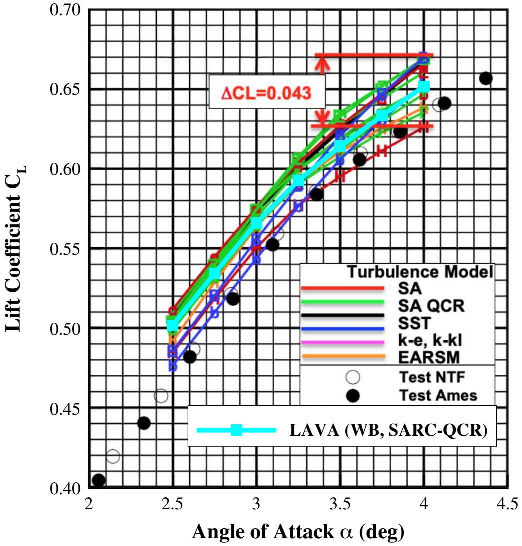

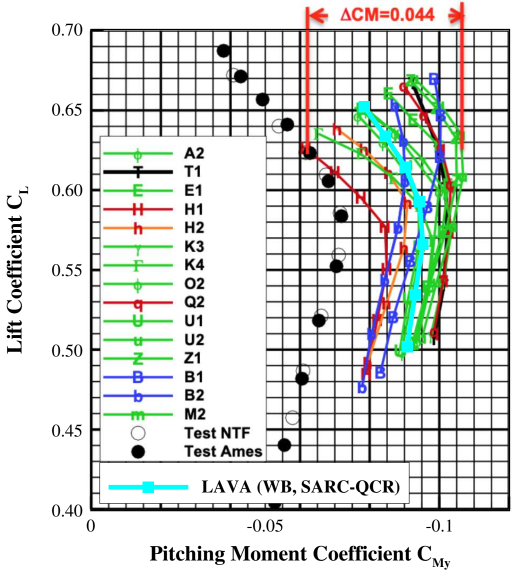

[3] doi.org/10.2514/1.C034409
[4] doi.org/10.2514/6.2012-707
[5] doi.org/10.2514/6.2012-3209

† It should be noted that the horizontal tail will increase the sensitivity to these effects

PART I

WIND TUNNEL DATABASE RUNS

Grid Topology

- Overset grids were created according to the guidelines from DPW-VI
- Grids were consistently refined to generate a family of 3 grids

Configuration	# Grid Points	Coarse	Medium	Fine
Clean	Total	21M	60M	156M
	Solve	16M	47M	122M
TCT	Total	30M	86M	224M
	Solve	23M	66M	173M

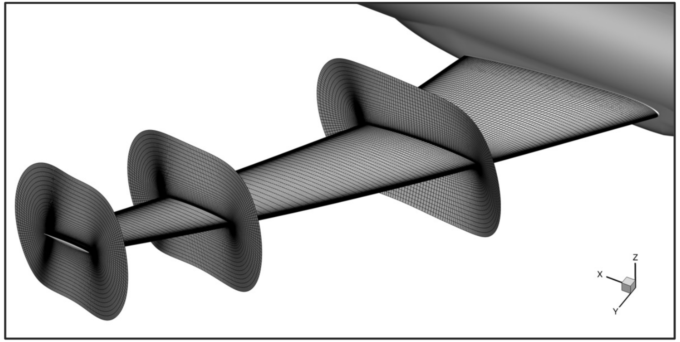

Wing O-grid topology detail

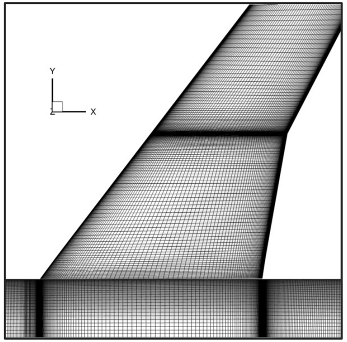

Wing surface grid

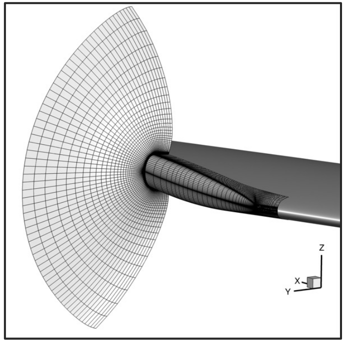

Wing tip cap grid

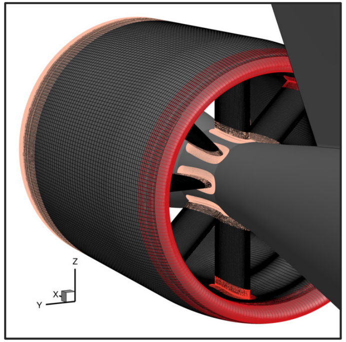

TCT grids

Grid Topology

- Overset grids were created according to the guidelines from DPW-VI
- Grids were consistently refined to generate a family of 3 grids

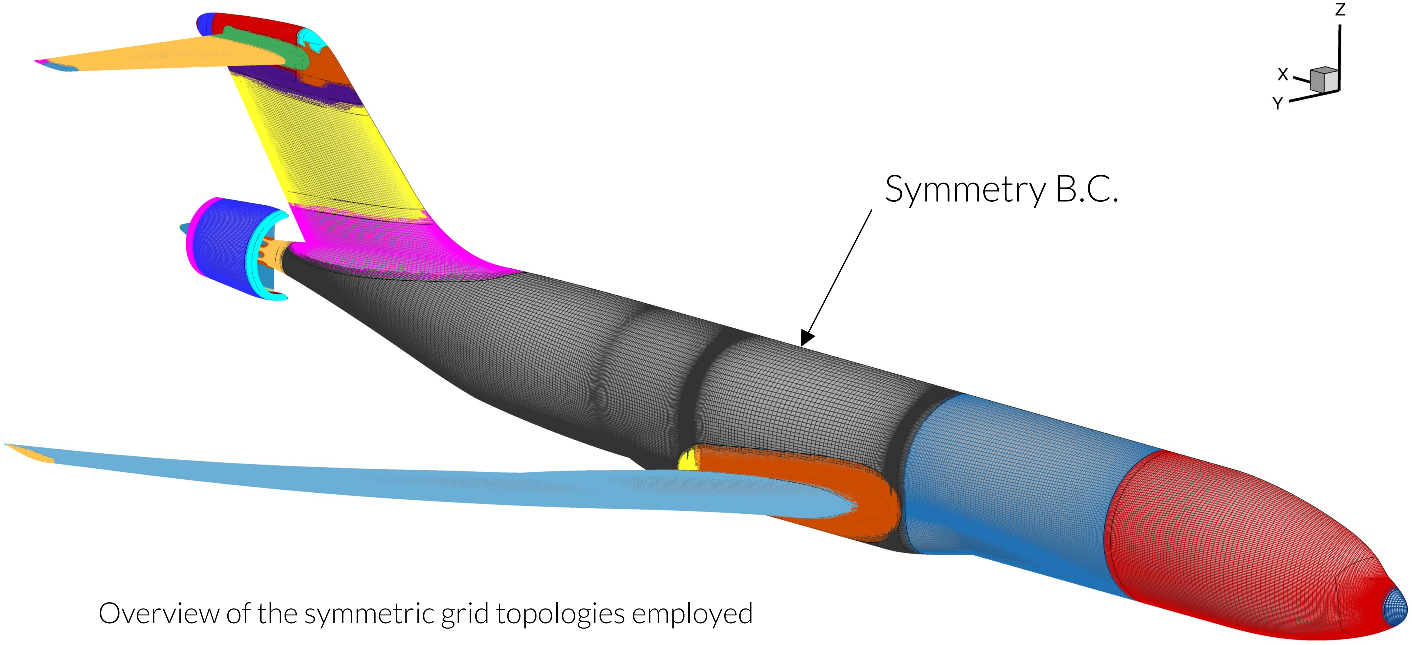

Overview of the symmetric grid topologies employed

Grid Topology

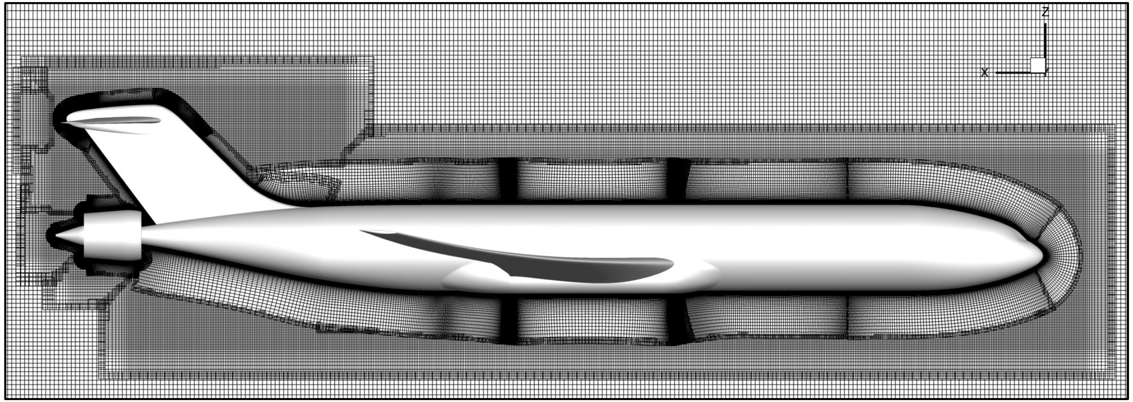

No-sting configuration (TCT-NS) volume grid cut.
Medium grid level.

Sting configuration (TCT-S) volume grid cut.
Medium grid level.

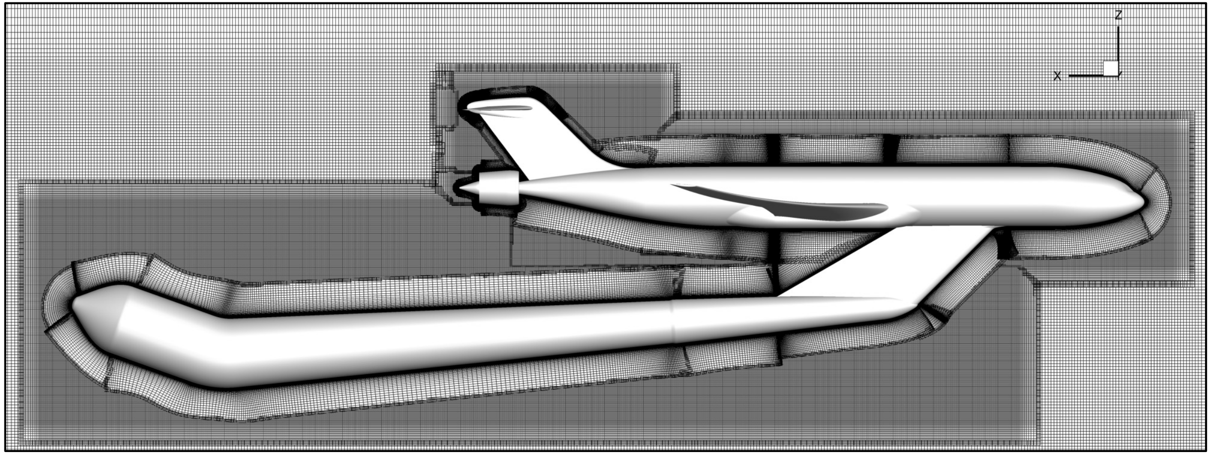

Grid Refinement Study

- Grid refinement study performed for condition
  - Re = 5M, Ma = 0.85 and AoA = 2°
- 2nd order convergence observed for C_D, little sensitivity seen in C_L with non-monotonic convergence with grid refinement

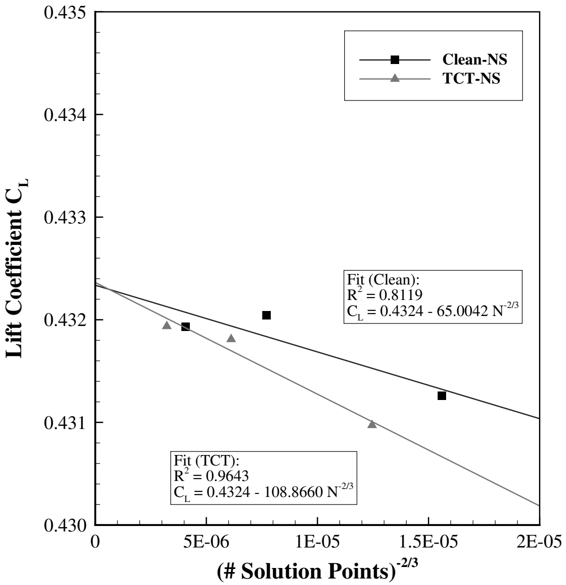

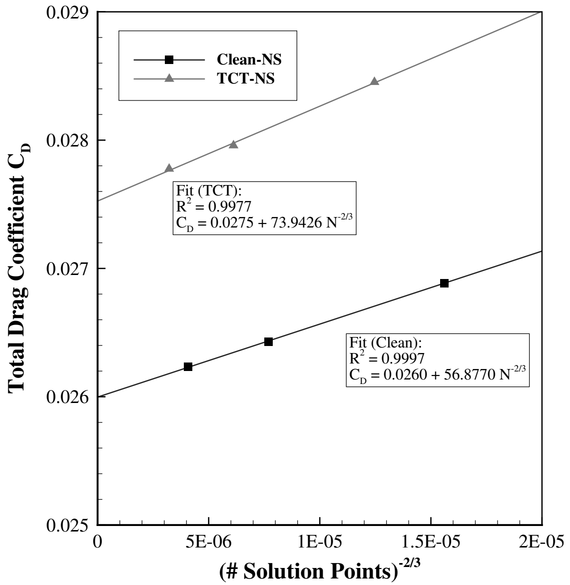

Grid Refinement Study

- Pitching moment coefficient also shows 2nd order convergence for both Clean and TCT-NS configurations, while the mass flow rate in TCT-NS case converges to an asymptotic value of 6.835 lbm/s

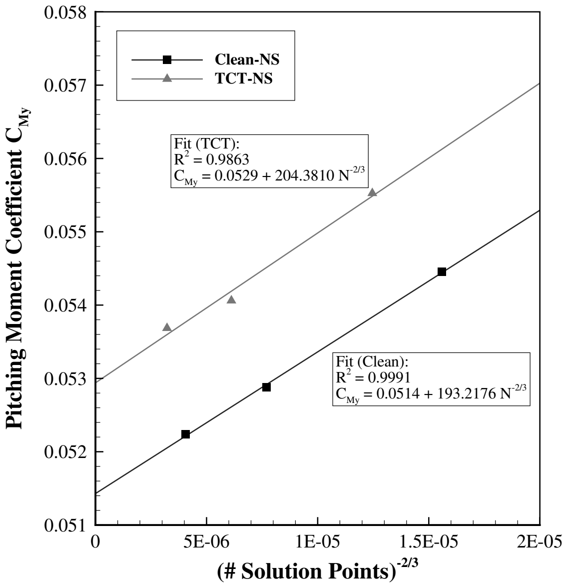

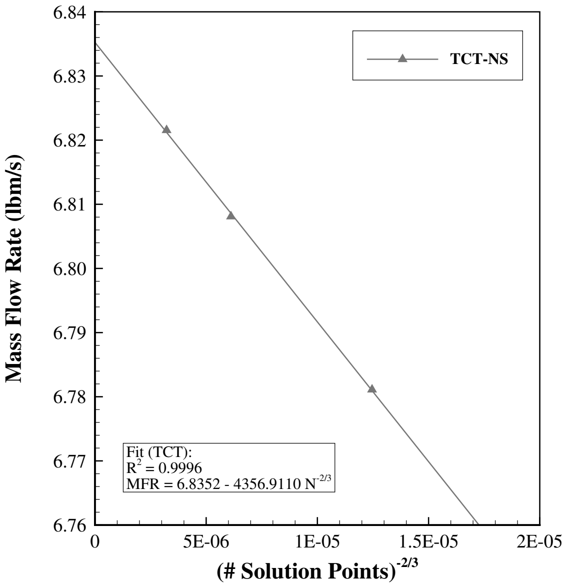

Flow Distortion Characterization

- Flow distortion is quantified according to the ARP1420 standard by measuring total pressure and flow angularity at the nacelle highlight
  - 40 probes located 45° apart along five radial locations defined by equal-area rings
- Flow angularity measures the angle of the velocity vector to the engine axis:

$$\theta_{\text{flow}} = \cos^{-1} \frac{\boldsymbol{V} \cdot \boldsymbol{e}_x}{|\boldsymbol{V}|}$$

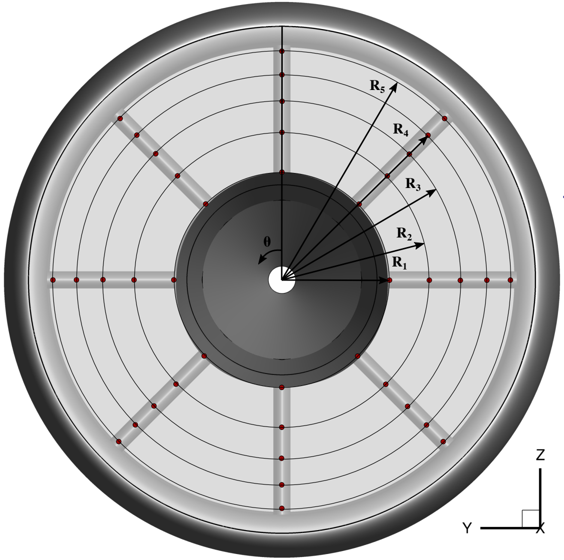

ARP1420 probe locations

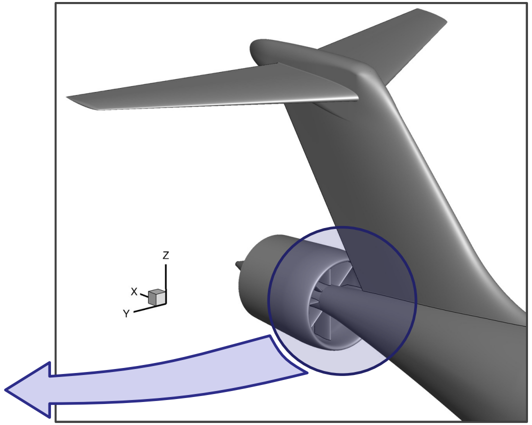

Flow-through aft-body

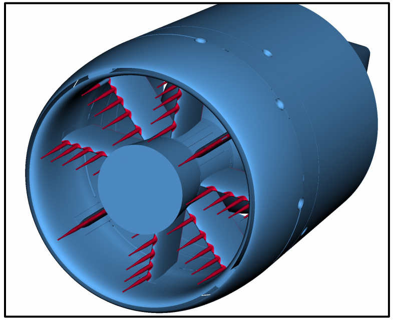
Wind tunnel probe geometry

Grid Refinement Study

- Very little sensitivity observed in nacelle highlight flow distortion metrics across the three grids, particularly between the medium and fine level grids
- Main grid-sensitive areas clustered around bottom half of the engine

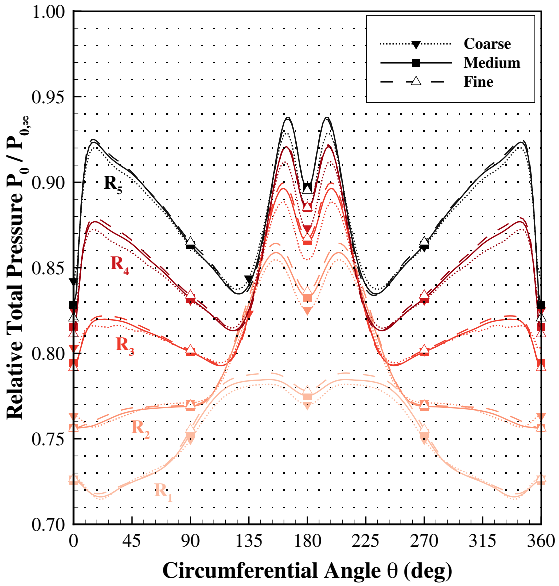

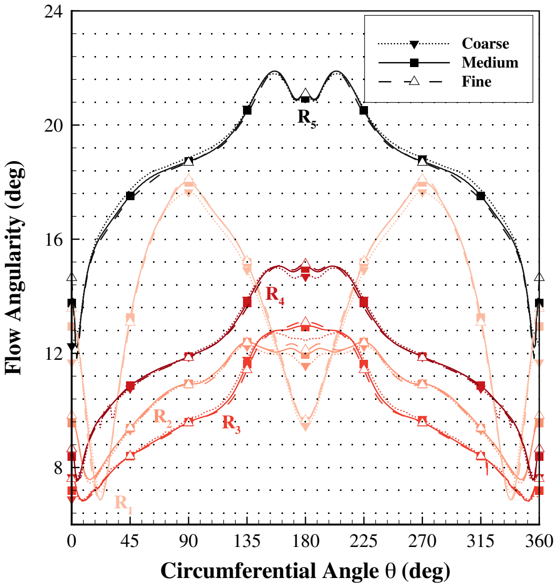

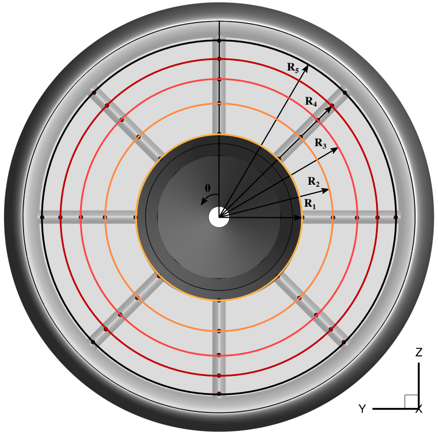

ARP1420 location color coded

Key Flow Distortion Mechanisms

- Total pressure minimum at around 0° corresponds to the losses occurring as the flow goes past the vertical tail

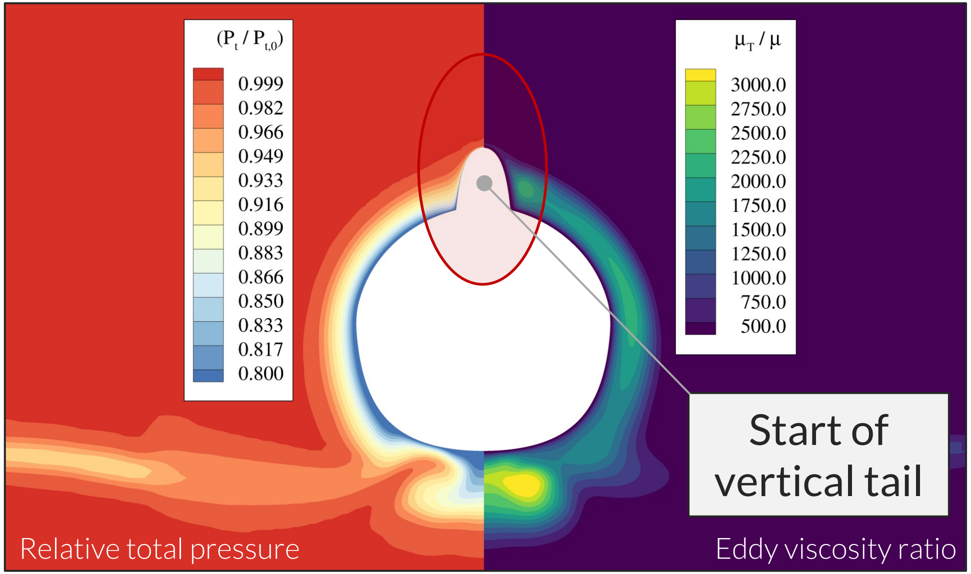

Streamwise cut downstream of the wing

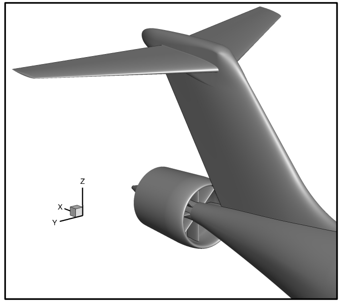

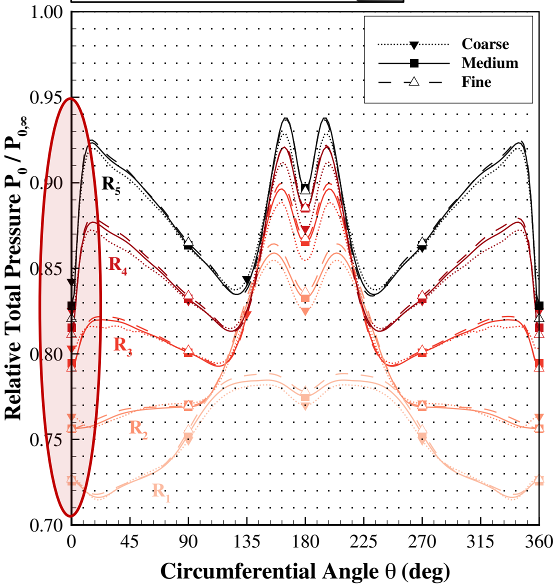

Key Flow Distortion Mechanisms

- Pressure losses occur as flow moves past the wing
- Fuselage upsweep vortices drive wake flow towards lower fuselage

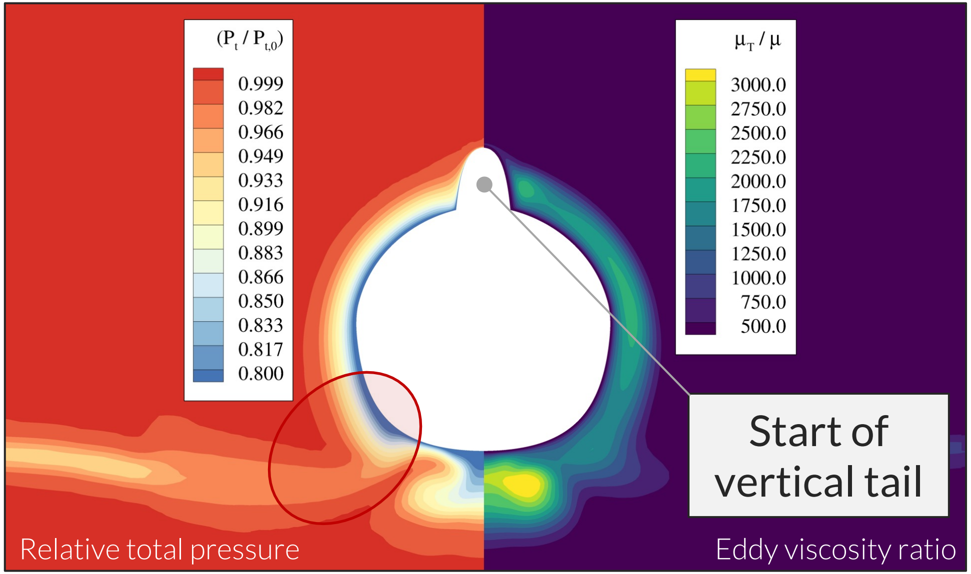

Streamwise cut downstream of the wing

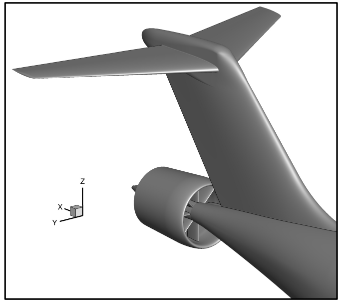

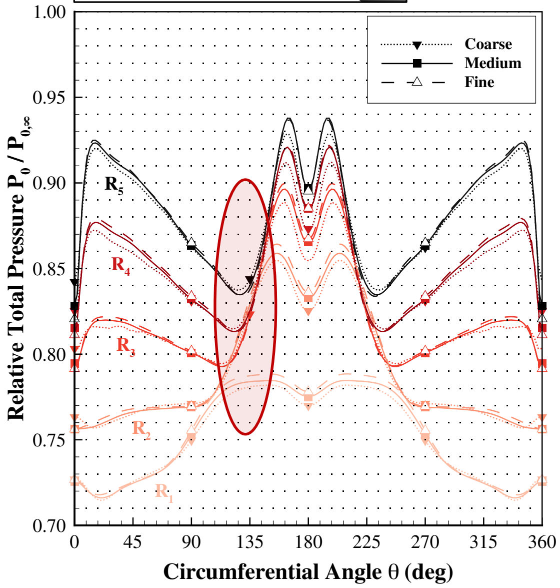

Key Flow Distortion Mechanisms

- Pressure losses occur as flow moves past the wing
- Fuselage upsweep vortices drive wake flow towards lower fuselage

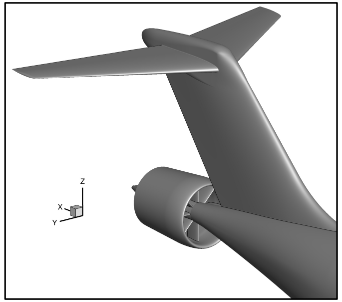

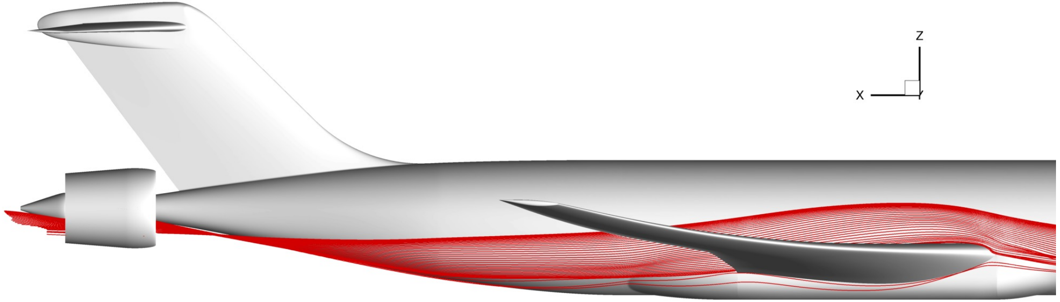

Streamlines over the wing

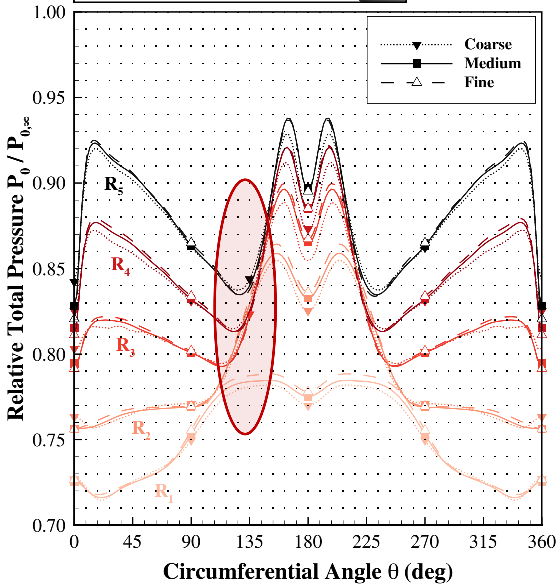

Key Flow Distortion Mechanisms

- Lower pressure region at $\theta = 180°$ caused by fuselage boundary layer getting pushed downwards by upsweep vortices

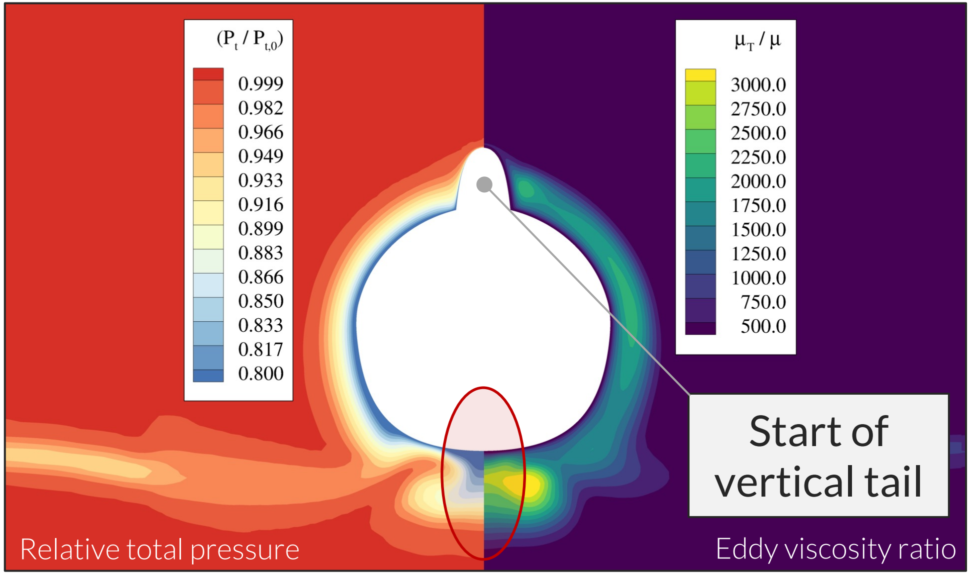

Streamwise cut downstream of the wing

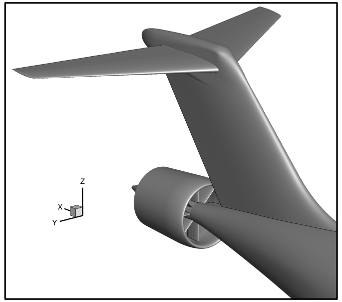

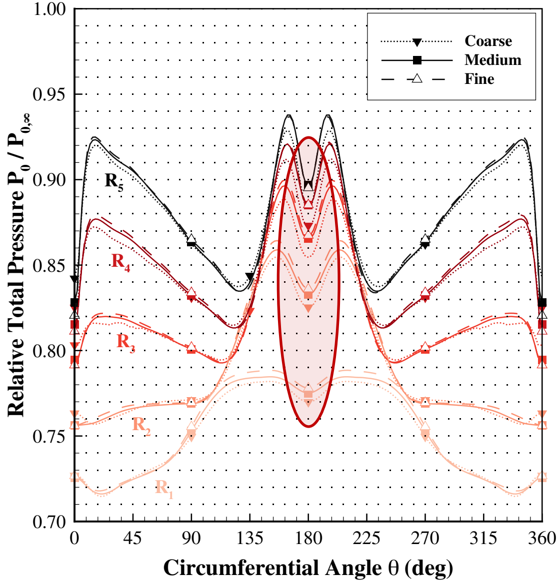

Key Flow Distortion Mechanisms

- Larger distortion profiles near the hub (R_1) and near the casing (R_5) – due to proximity to nacelle lip

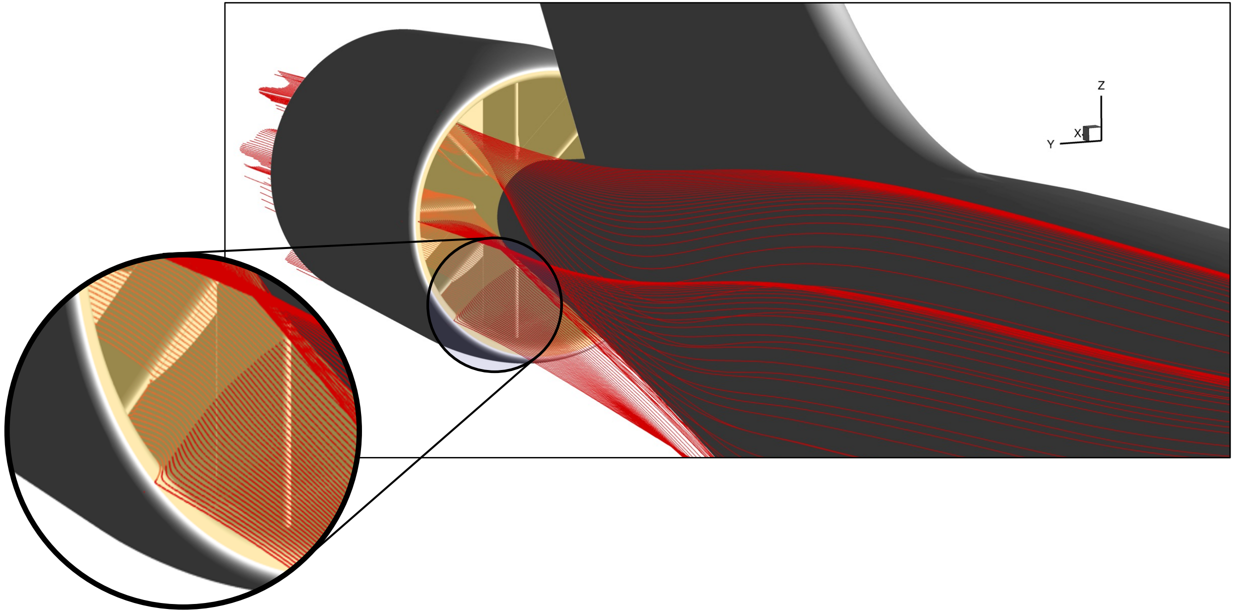

Close-up of nacelle lip region with streamlines, showing large radial distortion

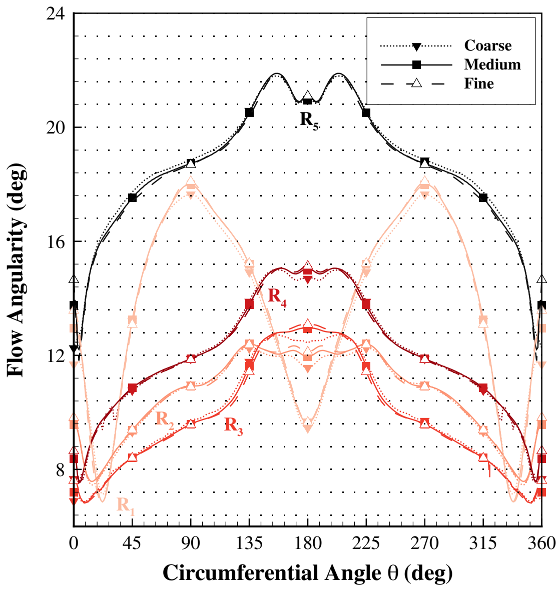

Simulation Initialization Procedure and Computational Cost

- Database alpha-sweeps were run by cold-starting the $\alpha = 0°$ case, and then warm-starting from the previous angle of attack

$$\mathbf{-4°} \leftarrow \mathbf{-3°} \leftarrow \mathbf{-2°} \leftarrow \mathbf{-1°} \leftarrow \mathbf{0°} \rightarrow \mathbf{1°} \rightarrow \mathbf{2°} \rightarrow \mathbf{3°}$$

- This method allowed for a computational cost savings of 45%, compared to cold-starting the entire 240 cases from freestream
- Entire database cost was around 48,000 core-hours, with each angle of attack case taking an average of 30 minutes on 400 Intel Skylake cores, or 200 core-hours
- For brevity, results will be shown for the Re = 10M condition only

Mach Number Sensitivity

- Little sensitivity observed in C_L between Clean and TCT configurations
- Mach 0.85 condition shows an increase in C_D with TCT installed, ranging from a minimum increase of 14 drag counts at $\alpha = 4°$, to a maximum of 17 drag counts at lower angles of attack

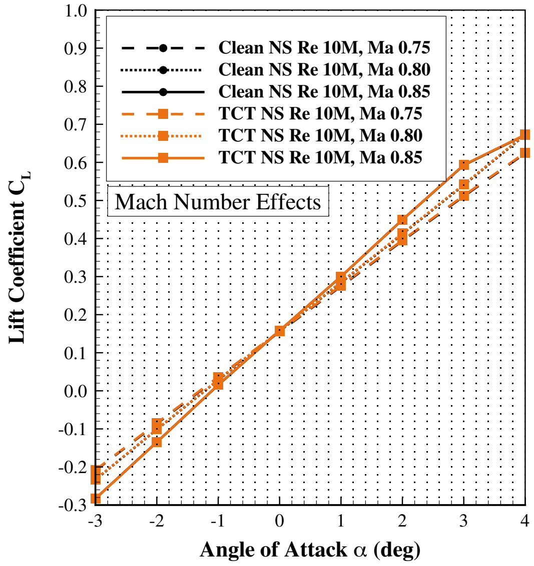

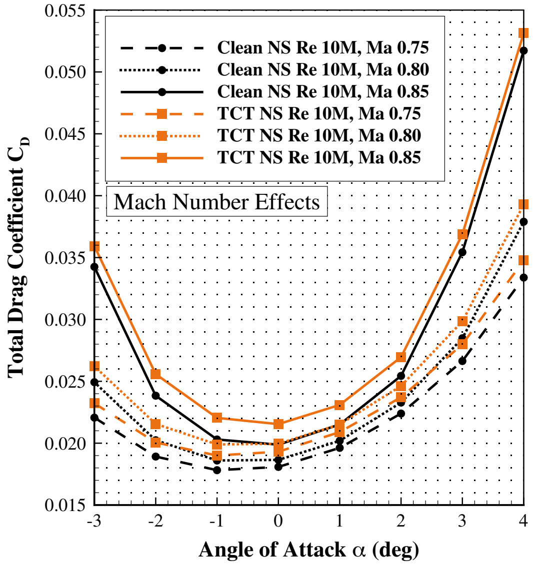

Mach Number Sensitivity

- Little sensitivity observed in C_{My} between Clean and TCT configurations
- Increase in pitching moment coefficient for 4° angle of attack case caused by appearance of small shocks in the upper surface of the horizontal tail

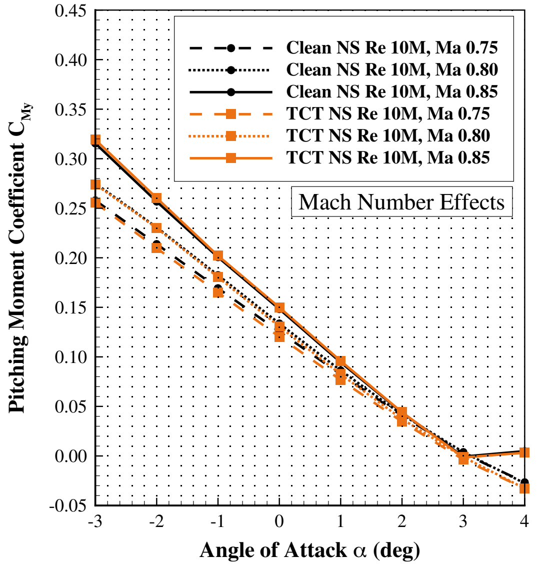

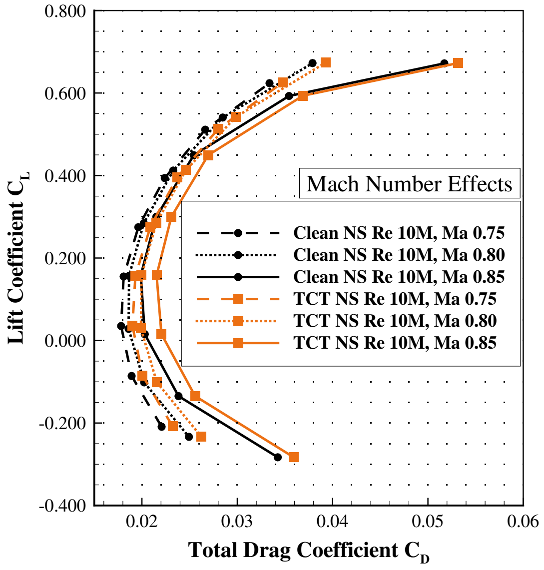

Sting Effects

- Presence of the sting plays a small role in C_L
- However, a significant decrease in C_D is observed when the sting is installed
  - This will be assessed in more detail once wind tunnel data is provided, and will depend on the kind of interference corrections that are performed on the data

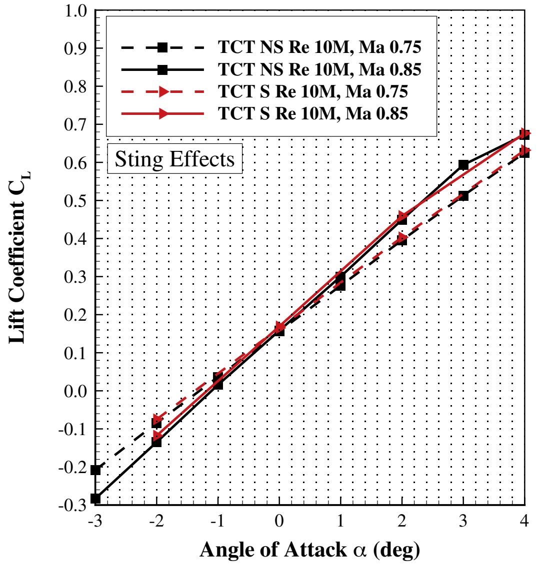

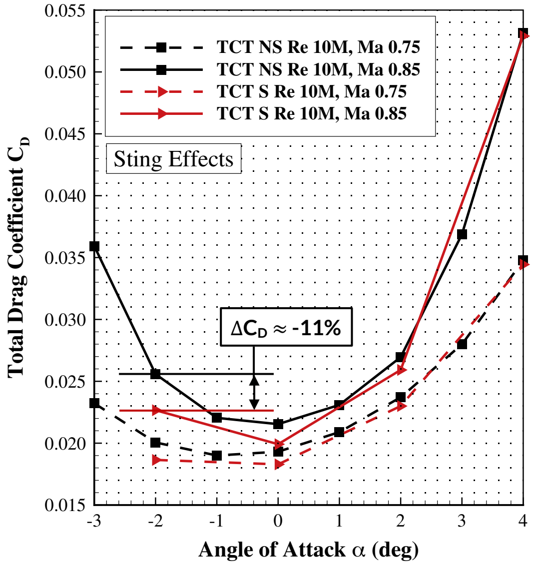

Sting Effects

- Small decrease in pitching moment coefficient C_{My}
- Significant impact on the measured mass flow rate through the tail-cone thruster
  - Sting interference/blockage effect lowers TCT mass flow rate by about 0.9% compared to free air

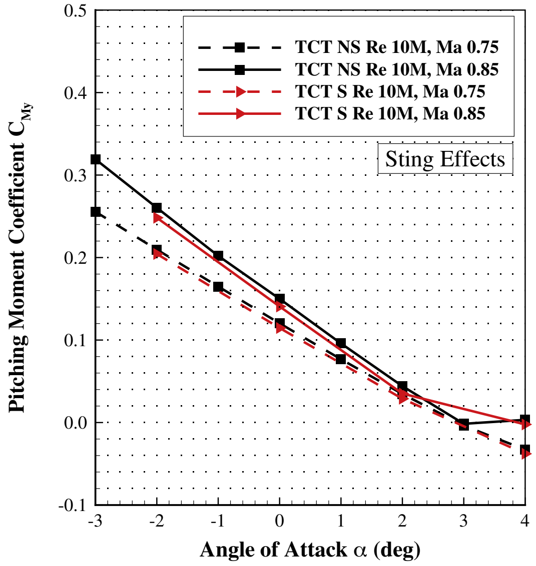

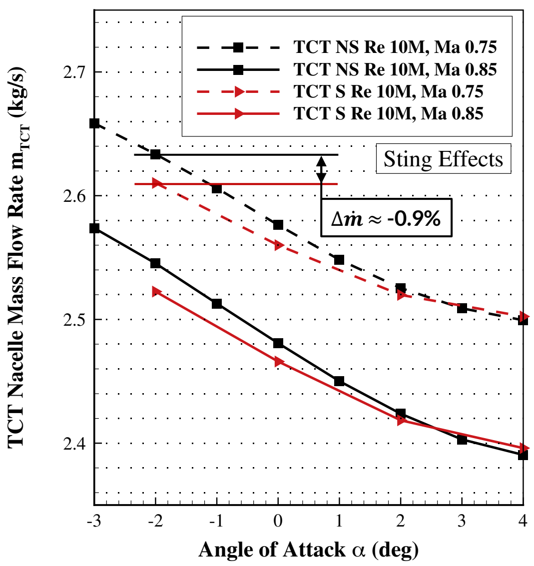

Sting Effects

- At α = 2°, the effects of the sting are present at the TCT inlet
  - Additional pressure losses observed across the circumference, but especially localized at 180°
  - Negligible effect on the flow angularity, except at the 180° location

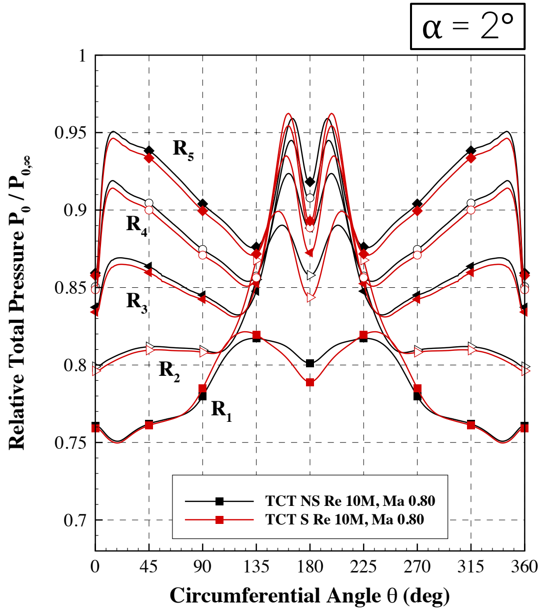

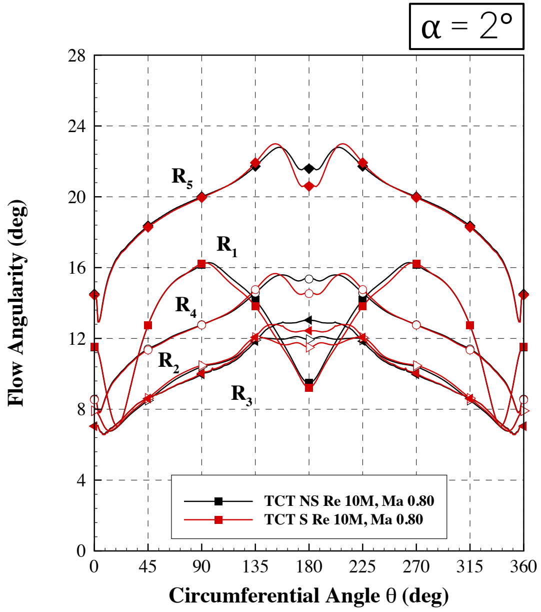

Mass Flow Plug Sensitivity

- Unique mass flow plugs allow simulations of different operating power levels
- Monotonic increase in C_L caused by higher *simulated thrust* and 2° angle of attack
- Similar C_D between -10% and Cruise MFP; 8 drag count increase with +10% MFP

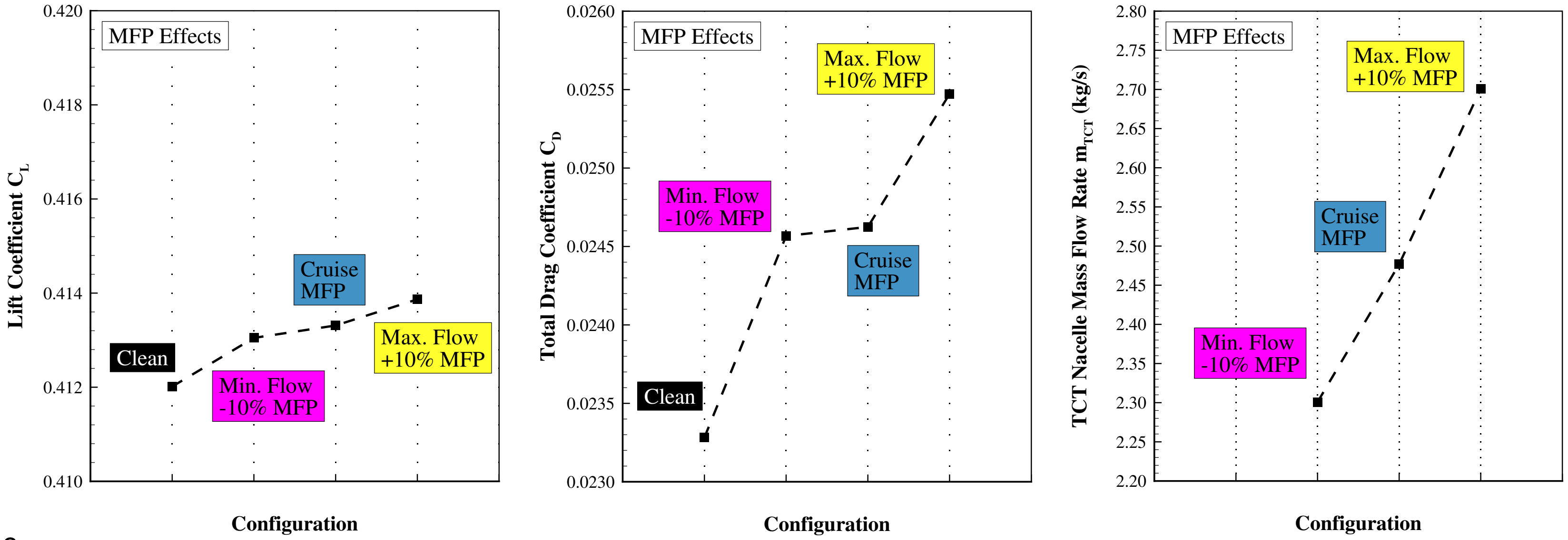

Mass Flow Plug Sensitivity

- Total pressure losses appear to be lower at higher TCT mass flow rate conditions
- However, there is a penalty in the flow angularity distortion when operating at higher simulated power levels

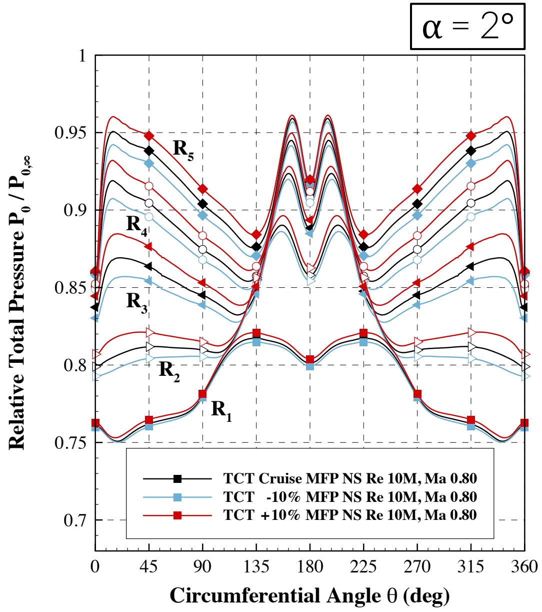

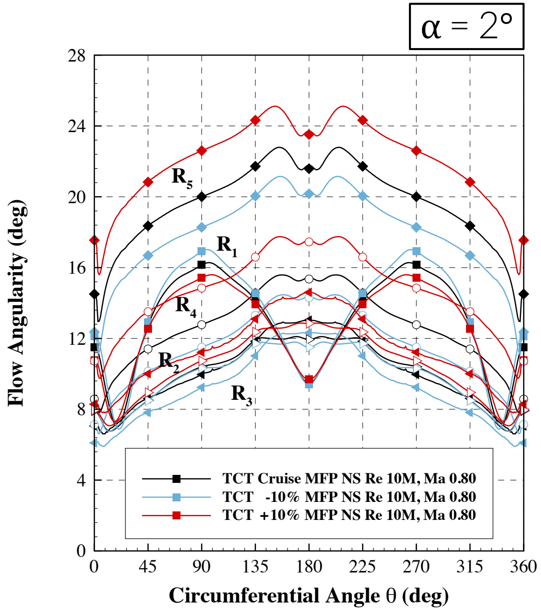

Flow Distortion Signature

- Nacelle highlight contours of relative total pressure emphasize distortion signature
- Low total pressure region around the hub corresponds to the fuselage boundary layer that is ingested; levels of flow distortion are high around top half of inlet at lower angles of attack, and high in lower half of inlet at higher angles of attack

$\alpha = -2°$

$\alpha = 4°$

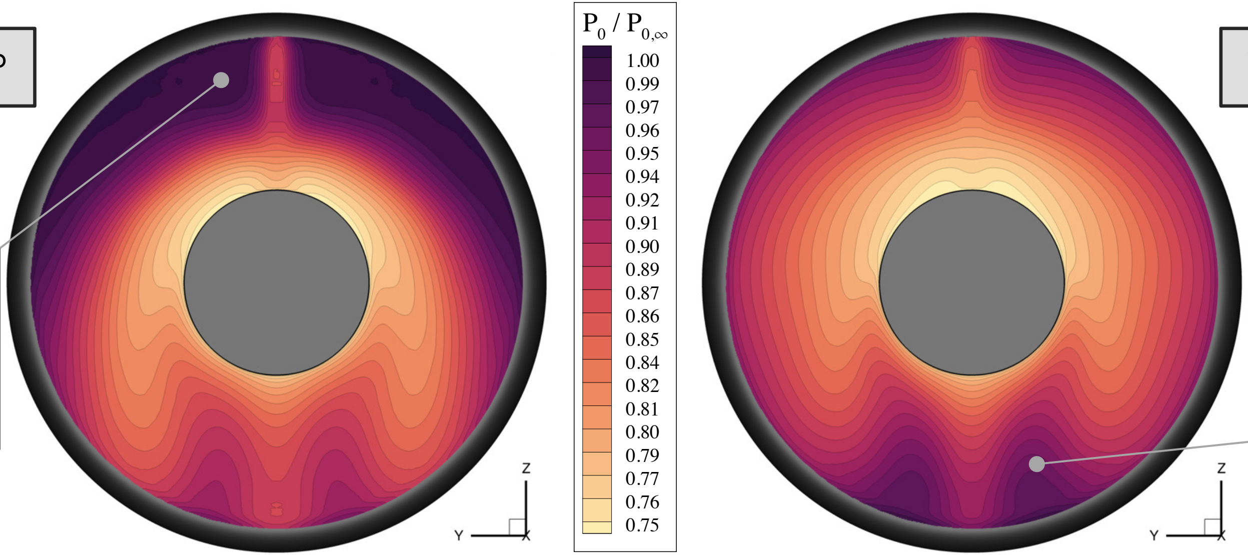

Ingestion of near-freestream flow at low angles of attack

Fuselage upsweep vortices introduce higher distortion at higher angles of attack

Flow Distortion Signature

- Little sensitivity observed for the flow angularity at the nacelle highlight with angle of attack
- Regions of high flow angularity at the bottom half of the inlet correspond to the fuselage upsweep vortices ingested by the TCT

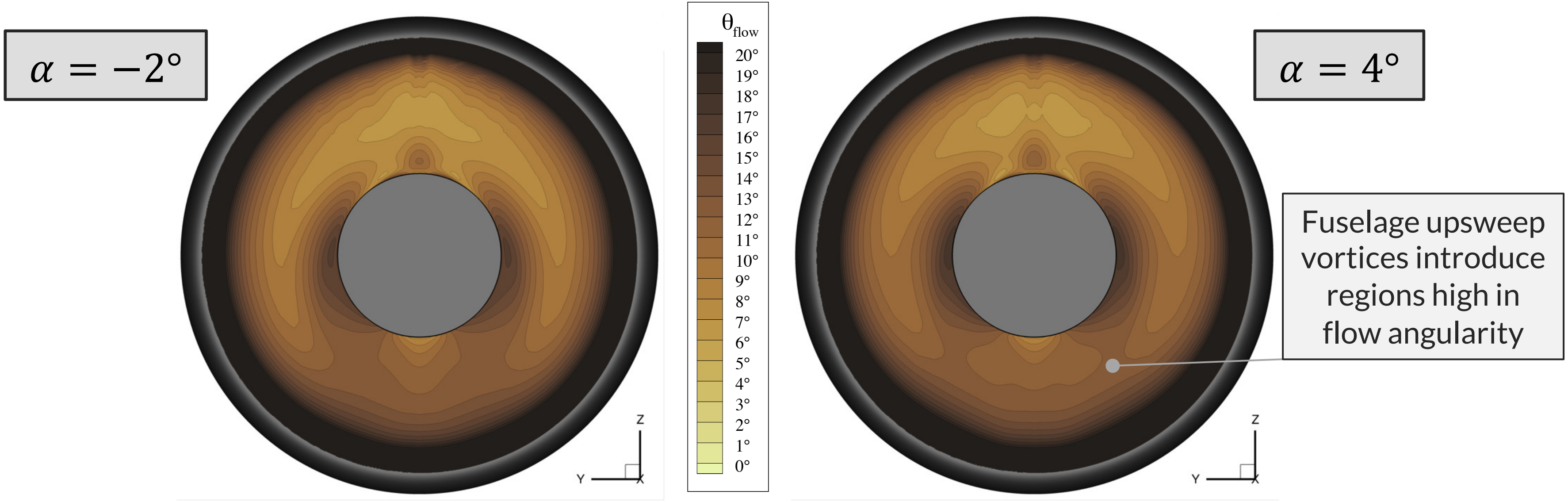

Flow Distortion Signature

- TCT inlet pressure contours vary significantly with angle of attack, emphasizing the range of inlet distortion conditions a distortion-tolerant fan must tolerate

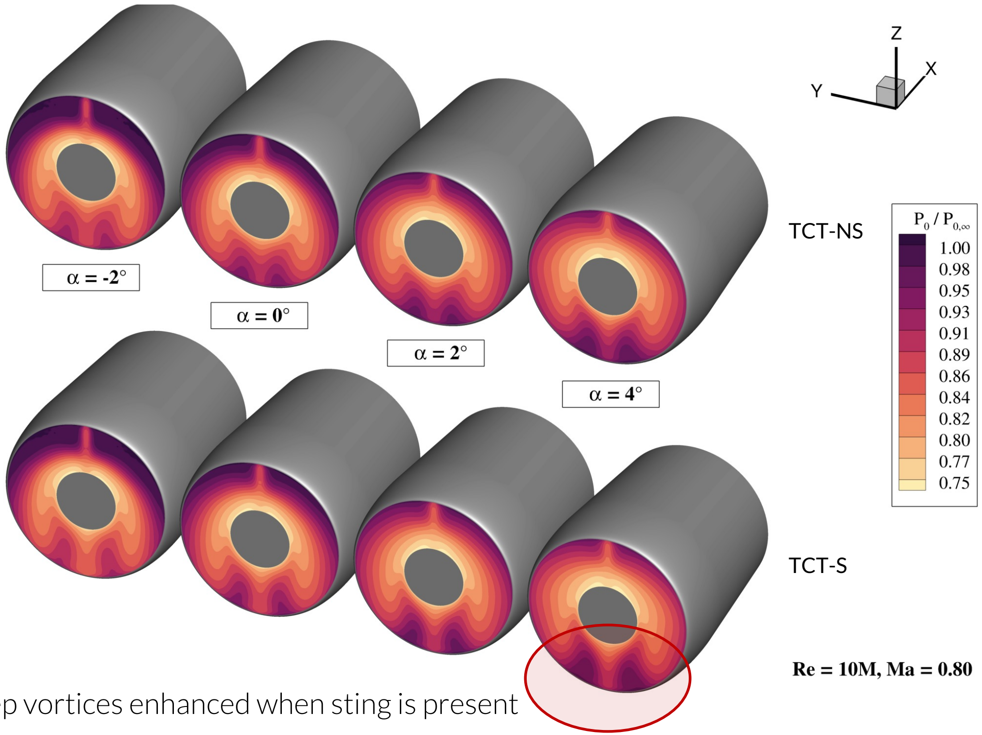

Effect of fuselage upsweep vortices enhanced when sting is present

Flow Distortion Signature

- Inlet flow angularity distortion shows little sensitivity to angle of attack

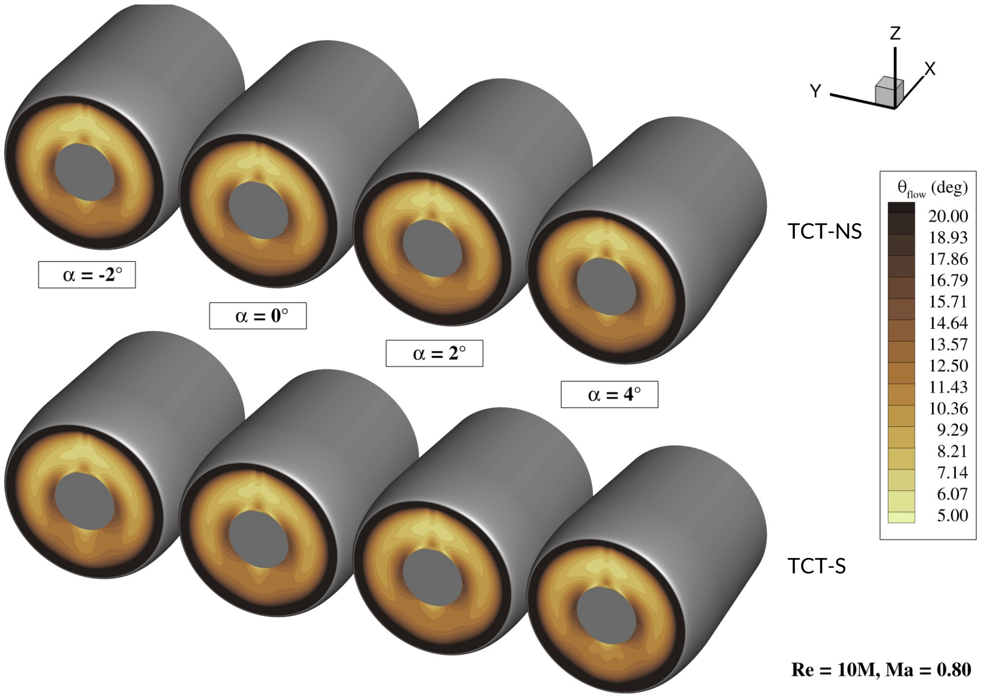

PART II

CFD SUPPORT FOR IGV DESIGN & INTEGRATION

CFD Support for IGV Design and Integration

- Levels of flow distortion observed need to be addressed in a powered setting to ensure good fan performance, even when a distortion-tolerant fan (DTF) is employed
- IGV design/integration effort between LAVA and TURBO teams
- Several iterations of the design significantly improved the flow distortion signature in front of the fan location
- Results will show the LAVA perspective of the collaboration between ARC and GRC teams

Latest IGV design
Courtesy of
Byung-Joon Lee et al.
(NASA GRC)

CFD Support for IGV Design and Integration

LAVA

TURBO

Initial IGV design

Geometry data sharing

Create grid system with IGVs

External flow field CFD using LAVA
- Incorporating an **actuator zone** model to simulate propulsor effects

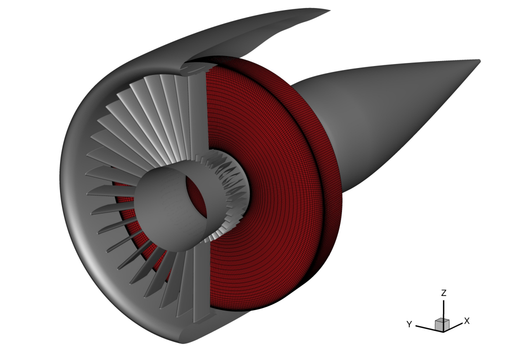

Actuator zone block with IGVs in LAVA

Flow field data sharing

Identify regions with poor flow behavior

Estimate performance metrics

Performance metrics met?

Yes

Final IGV design

No

New IGV design

Geometry data sharing

CFD Support for IGV Design and Integration

- Initial IGV design* used as start point showed separated regions and choked flow

15% Span

75% Span

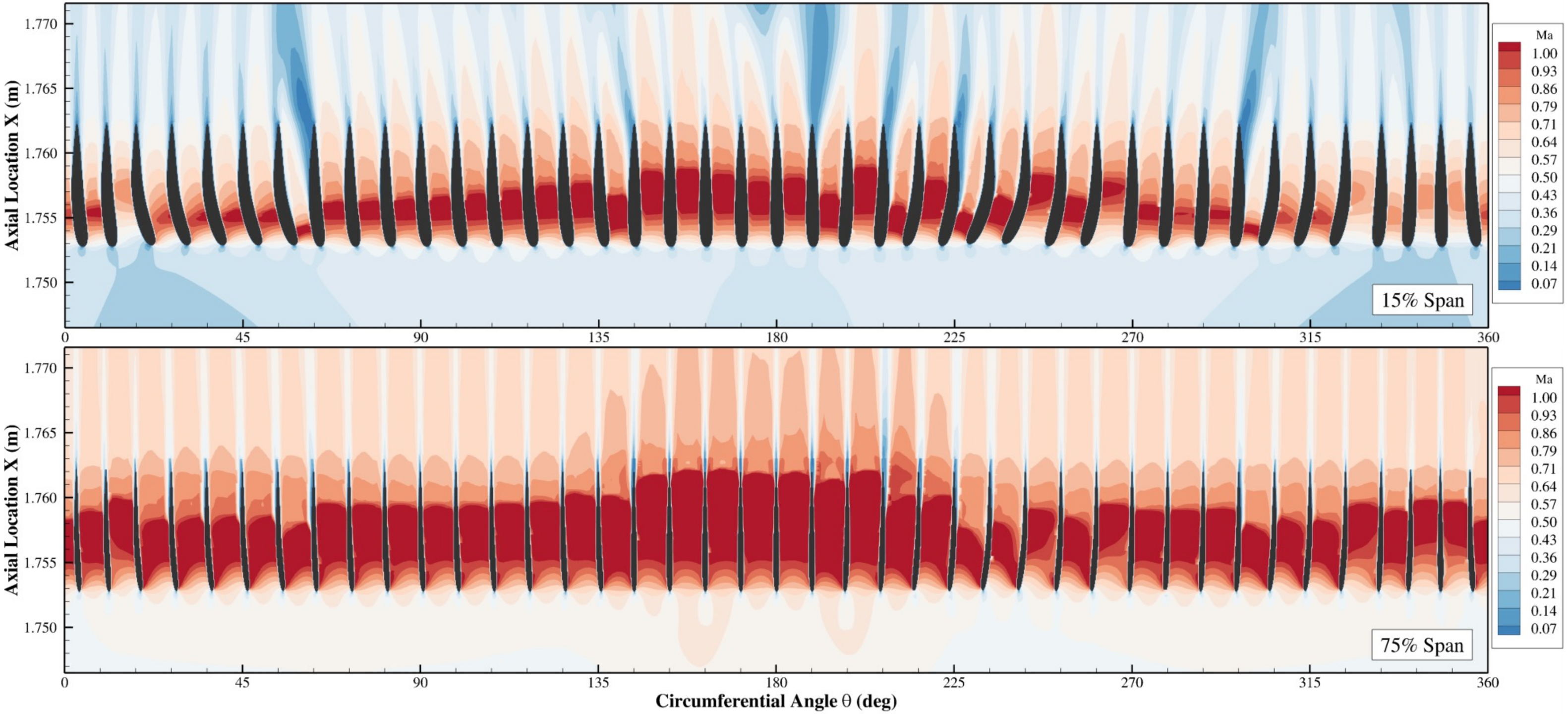

*IGV design performed by Byung-Joon Lee et al. (NASA GRC)

CFD Support for IGV Design and Integration

- Strong shocks eliminated in latest iteration*, and flow is aligned with axial direction

15% Span

75% Span

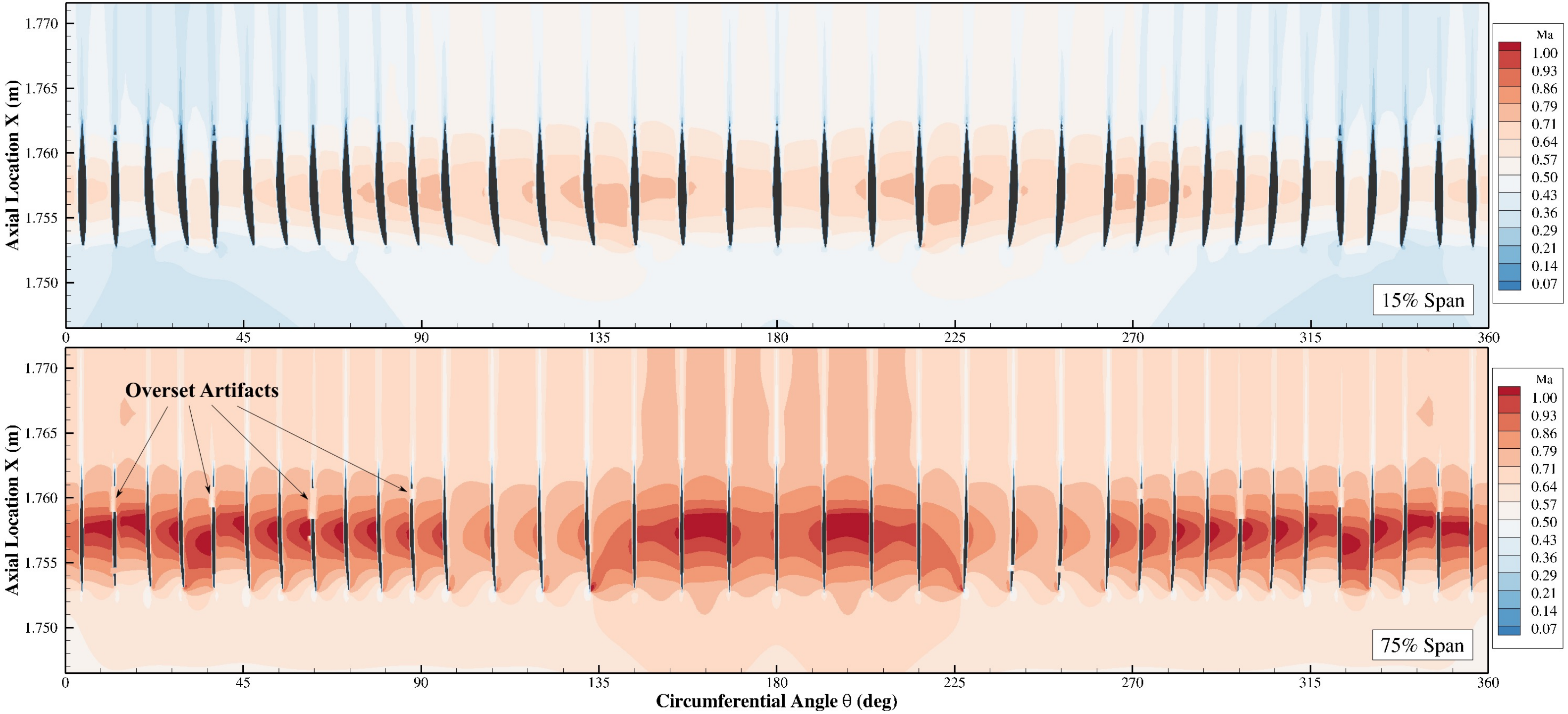

*IGV design performed by Byung-Joon Lee et al. (NASA GRC)

CFD Support for IGV Design and Integration

- More uniform total pressure distribution is observed at the aerodynamic interface plane (AIP) when IGVs are installed, especially near the hub in the bottom half of the profile, indicating the combined effect of wing downwash and fuselage upsweep has been mitigated

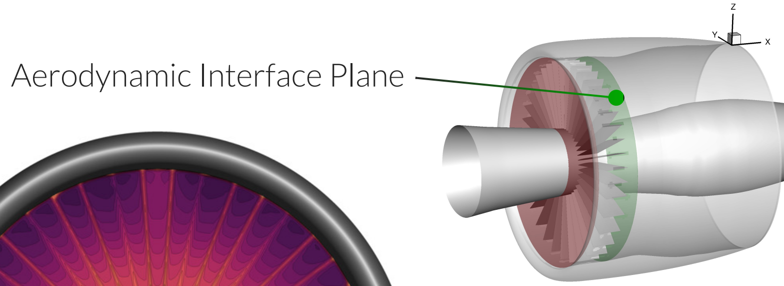

Large distortion induced by fuselage upsweep vortices

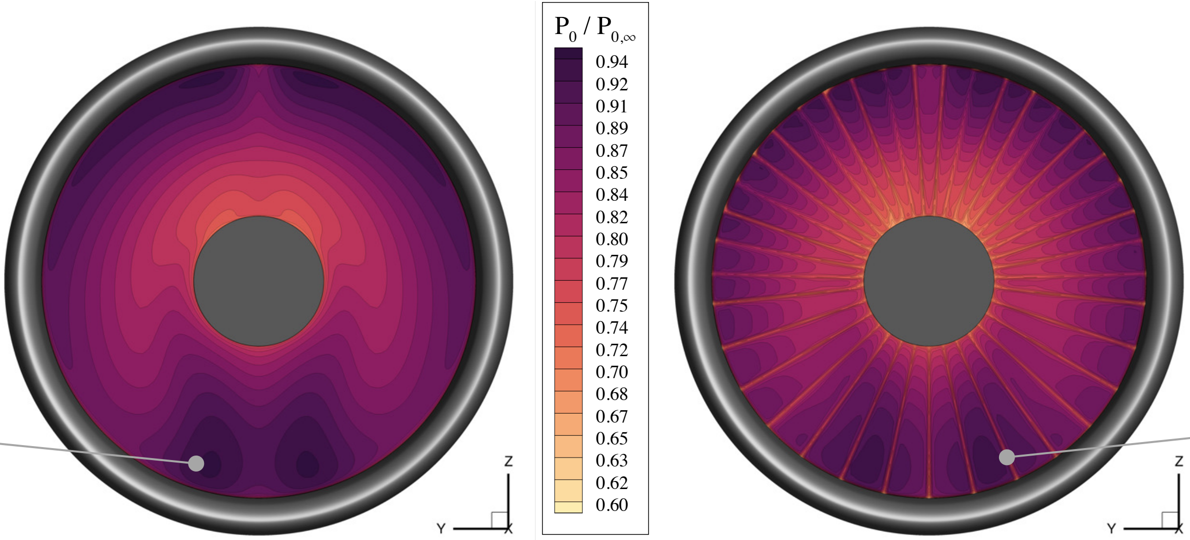

Distortion is mitigated by introduction of IGV system*

*IGV design performed by Byung-Joon Lee et al. (NASA GRC)

CFD Support for IGV Design and Integration

- Differences may be quantified along equal-area rings defined by ARP1420 standard at the AIP section
- Localized pressure drops observed along IGV* blade wakes result in a maximum integrated total pressure loss along the ring of 3.3%

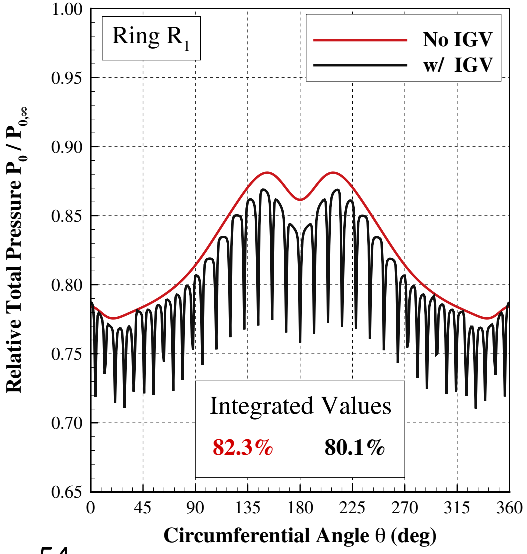

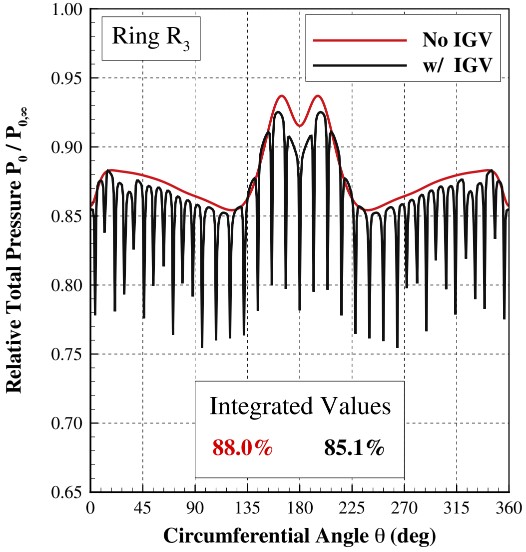

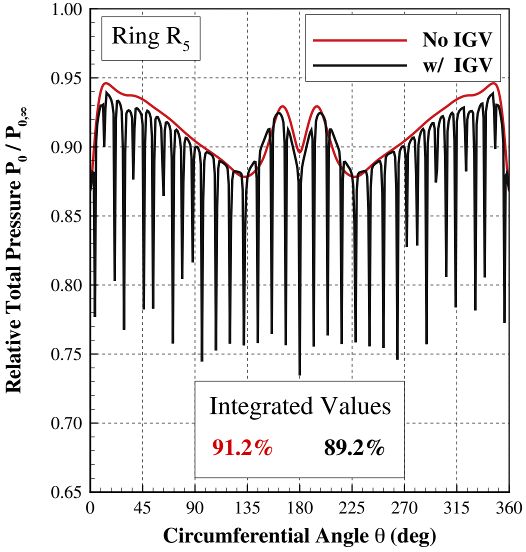

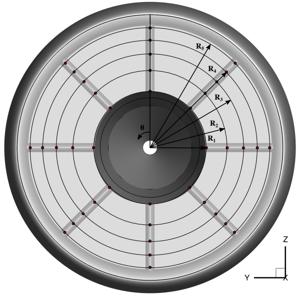

ARP1420 probe locations

*IGV design performed by Byung-Joon Lee et al. (NASA GRC)

CFD Support for IGV Design and Integration

- Large distortion region around the hub is substantially mitigated by IGV design*
- A significantly more uniform circumferential profile is observed with the IGVs, which will benefit DTF fan performance

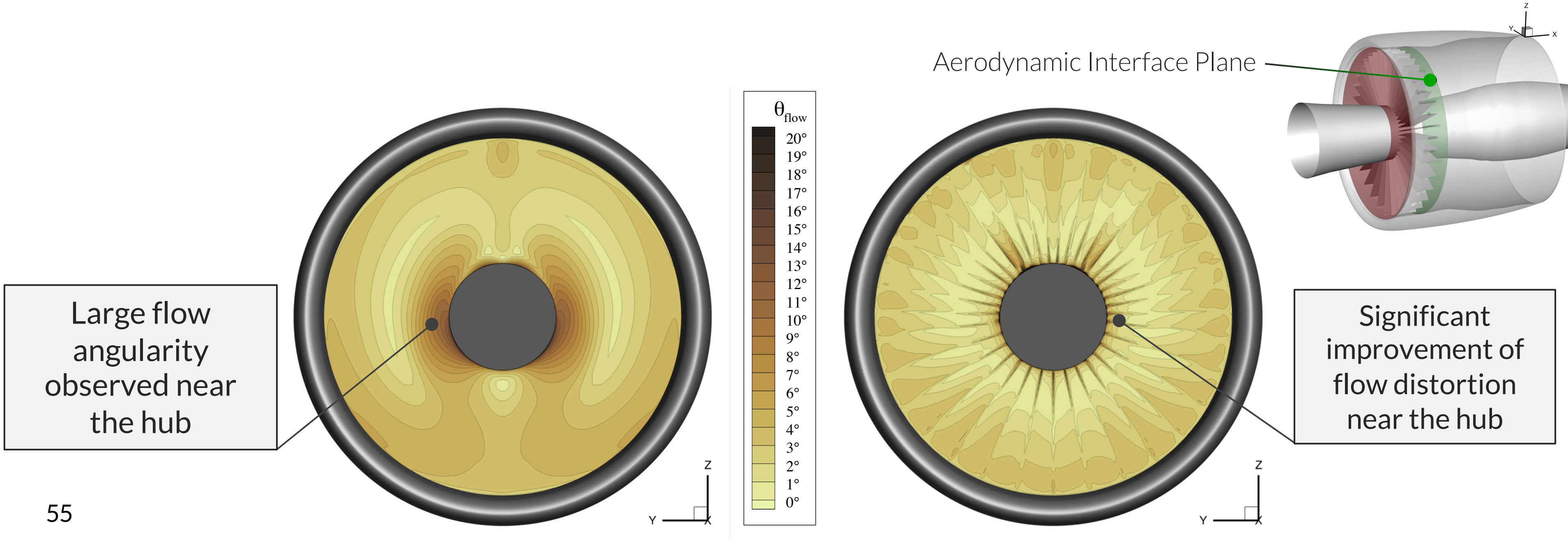

*IGV design performed by Byung-Joon Lee et al. (NASA GRC)

CFD Support for IGV Design and Integration

- Improvement near the hub is visible in ring R_1 plot, and is quantified with a 76% reduction in the integrated flow angularity metric
- Other profiles also see improvements with more uniform distribution

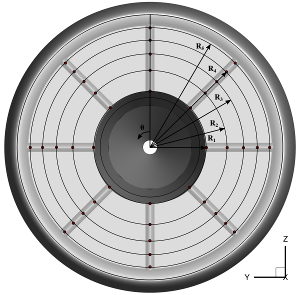

ARP1420 probe locations

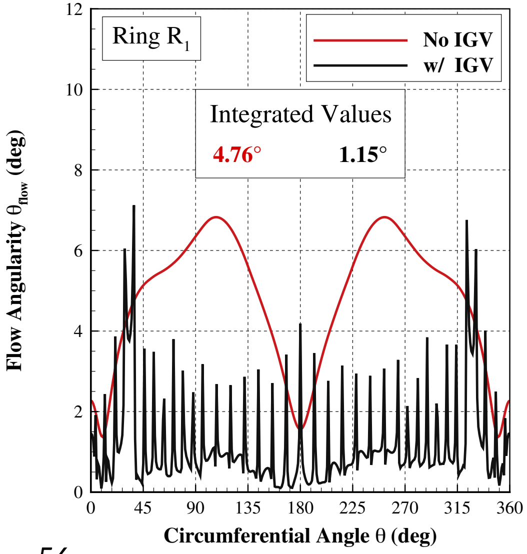

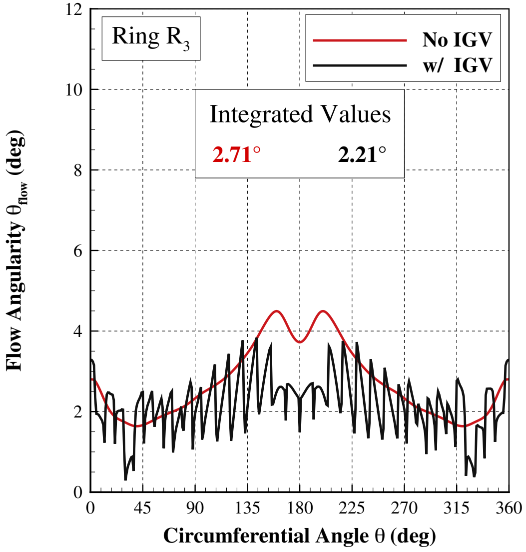

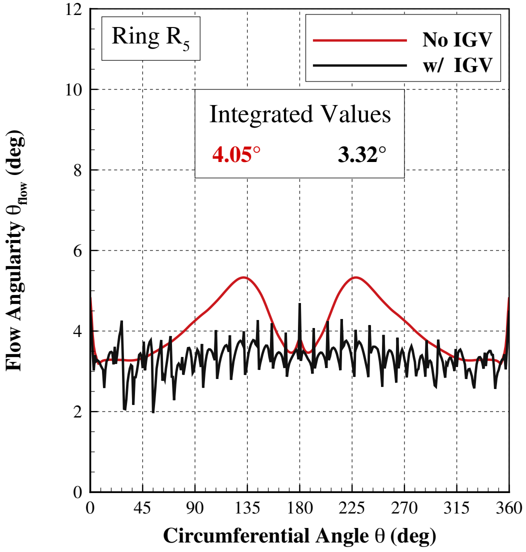

*IGV design performed by Byung-Joon Lee et al. (NASA GRC)

Propulsor Model Thrust Profile Sensitivity Study

- Tested more realistic radially-varying thrust profiles in the actuator zone model to account for blade hub and tip losses
  - Goldstein Optimum – derived from vortex theory under idealized assumptions
  - Custom Profile – obtained directly from an internal performance analysis on a fan

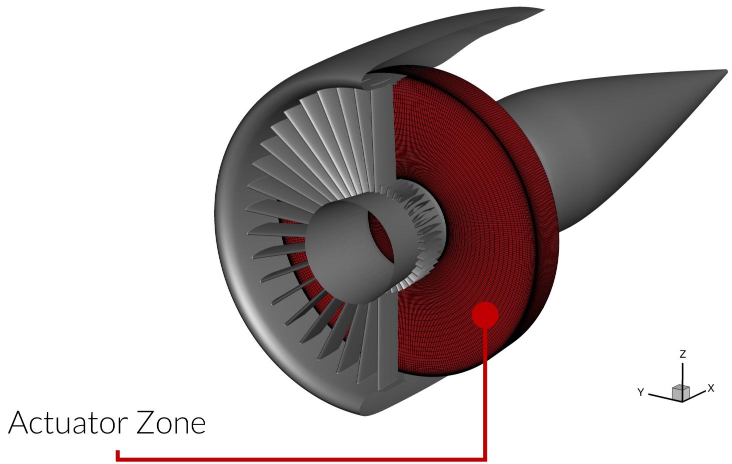

Actuator zone block with IGVs in LAVA

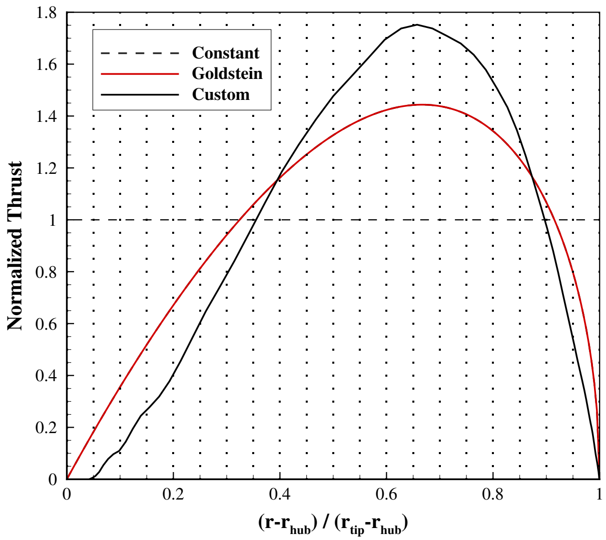

Propulsor Model Thrust Profile Sensitivity Study

- Differences in total pressure distortion between the three profiles almost entirely bound by 1%, showing little sensitivity to radial thrust variation
- Slight drop in total pressure likely caused by higher velocities induced by Goldstein and Custom thrust profiles as flow goes past IGVs

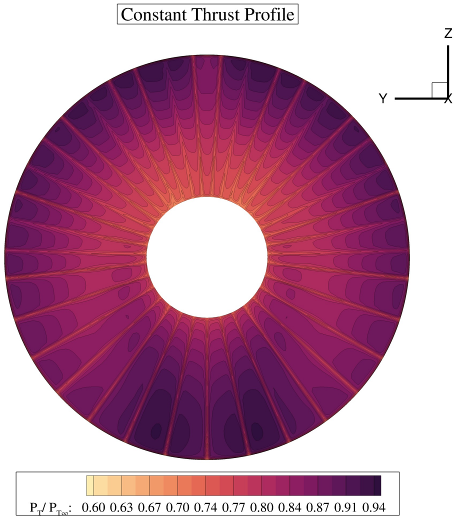

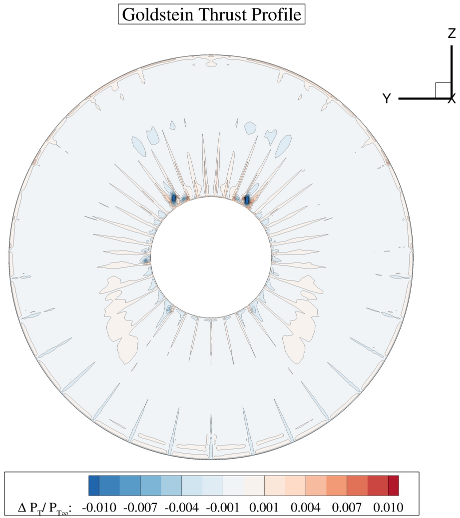

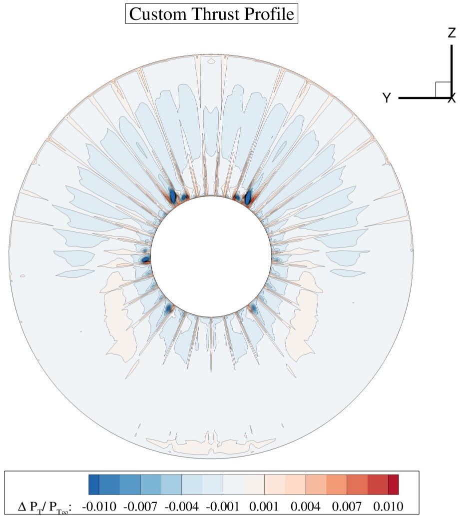

Propulsor Model Thrust Profile Sensitivity Study

- Lower thrust values of Goldstein and Custom profiles result in higher flow angularity distortion near the blade hub and tip regions
- Lower momentum imparted by the actuator zone makes the IGVs less effective at counteracting the flow distortion that they ingest

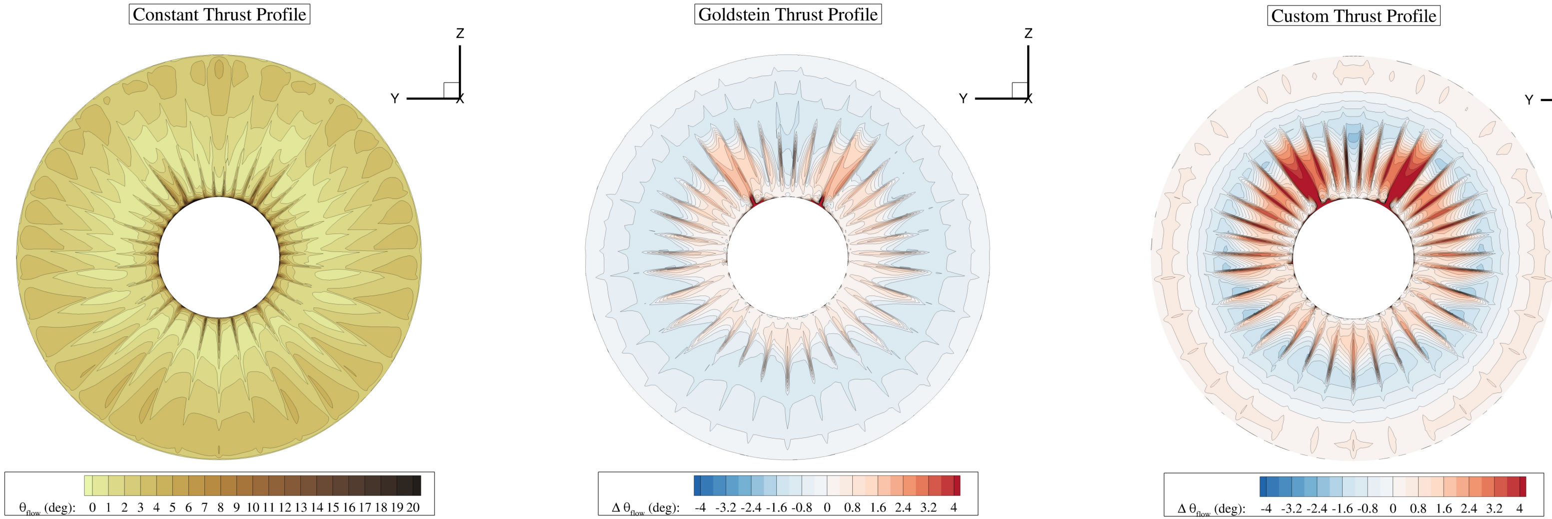

SUMMARY

Summary and Next Steps

- RANS simulation database consisting of 240 cases was generated using LAVA for comparison with NTF test campaign on the CRM-TCT variant, at a computational cost of roughly 48,000 core-hours
- Sensitivities to angle of attack, flow conditions, engine operating power level and wind tunnel mounting hardware were analyzed and documented
- Collaboration between NASA's ARC and GRC teams has resulted in an IGV system capable of reducing engine inlet flow angularity distortion by up to 76% close to the hub, at a maximum integrated pressure loss penalty of around 3.3%
- Resulting Type-II BLI system with IGVs will continue undergoing design improvements as it is integrated into future aircraft concepts, such as the NASA Transonic Truss-Braced Wing (TTBW)

Acknowledgements

- Research supported by NASA's Advanced Air Transport Technology (AATT) project
- Computer time provided by the NASA Advanced Supercomputing (NAS) facility at NASA ARC
- Special thanks to:
  - Byung Joon Lee, May-Fun Liou and Julia Stephens from NASA GRC for the IGV design/integration collaboration
  - Michael Bozeman from NASA LaRC for the code-to-code comparison between LAVA and USM3D on the database results
  - Shishir Pandya from NASA ARC for providing technical leadership and fruitful discussions
  - James Jensen, Gaetan Kenway, Jeffrey Housman and Gerrit Stich from the LAVA team for their contributions to the work

Thank you for your attention!

Questions:
luismsfern@nasa.gov
cetin.c.kiris@nasa.gov

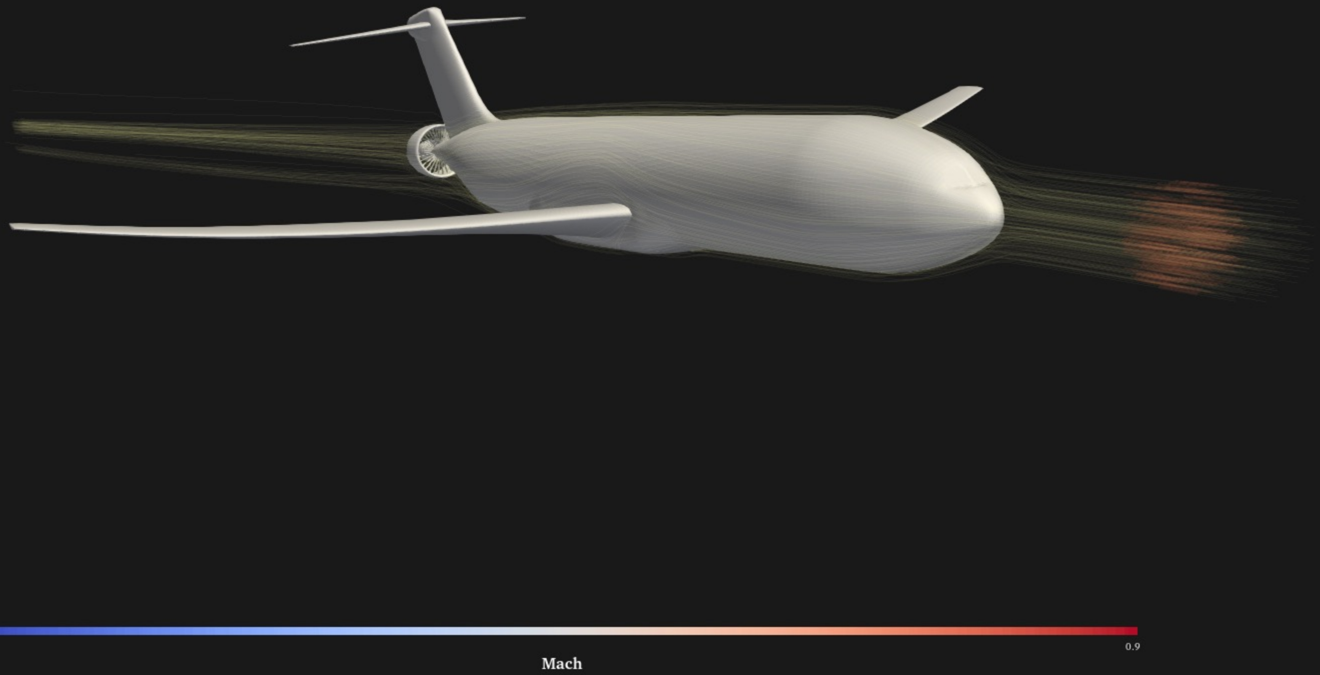

BACKUP SLIDES

Moment Coefficient Increase at Mach 0.85, α = 3°

- Appearance of shocks in the upper surface of the horizontal tail for condition Mach 0.85, α = 3° explains the increase in moment coefficient observed

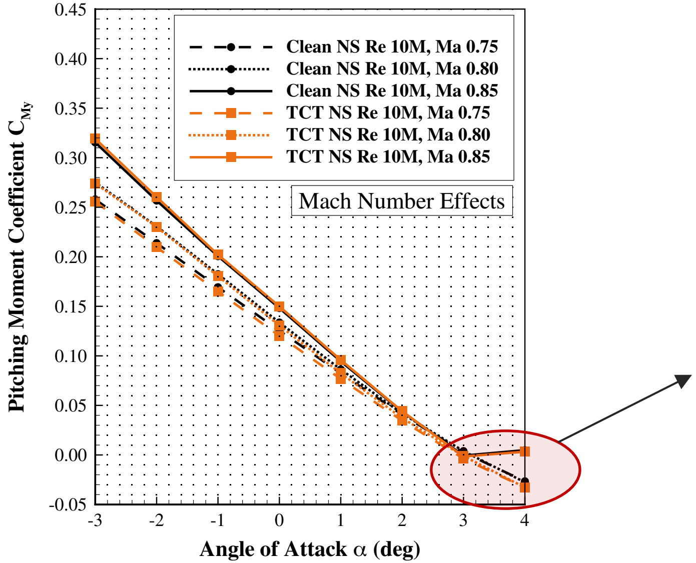

Increase in moment coefficient corresponding to a nose-up tendency at Mach 0.85

Moment Coefficient Increase at Mach 0.85, α = 3°

- Appearance of shocks in the upper surface of the horizontal tail for condition Mach 0.85, α = 3° explains the increase in moment coefficient observed

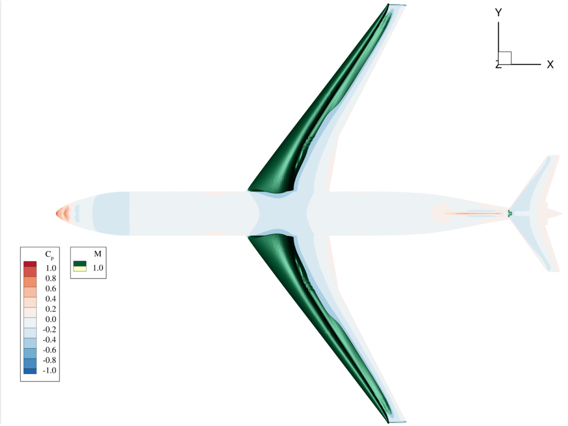

Re = 5M, Ma = 0.80, α = 4°

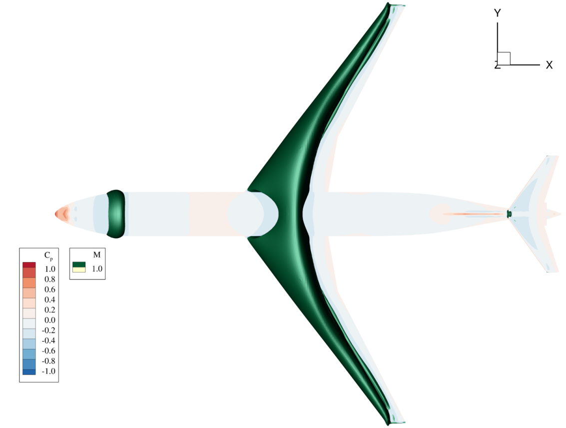

Re = 5M, Ma = 0.85, α = 3°

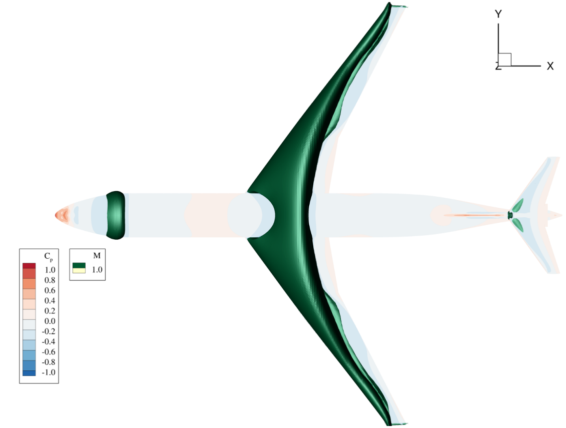

Re = 5M, Ma = 0.85, α = 4°